AGU PUBLICATIONS

Tectonics

RESEARCH ARTICLE
10.1002/2016TC004230

The tectonics of the western Ordos Plateau, Ningxia, China: Slip rates on the Luoshan and East Helanshan Faults

Timothy A. Middleton[1], Richard T. Walker[1], Dylan H. Rood[2,3], Edward J. Rhodes[4], Barry Parsons[1], Qiyun Lei[5], John R. Elliott[1], Zhikun Ren[6], and Yu Zhou[1]

[1]COMET, Department of Earth Sciences, University of Oxford, Oxford, UK, [2]Department of Earth Science and Engineering, Imperial College London, South Kensington Campus, London, UK, [3]AMS Laboratory, Scottish Universities Environmental Research Centre, East Kilbride, UK, [4]Department of Geography, University of Sheffield, Sheffield, UK, [5]Ningxia Seismological Bureau, Yinchuan, China, [6]State Key Laboratory for Earthquake Dynamics, Institute of Geology, China Earthquake Administration, Beijing, China

Key Points:
- Right-lateral slip rate on the Luoshan Fault is 4.3 ± 0.4 mm/a
- Throw rate on the East Helanshan Fault is <0.6 ± 0.1 mm/a
- Predominant motion in western Ordos is right-lateral strike slip, supporting anticlockwise rotation of the whole plateau

Supporting Information:
- Supporting Information S1

Correspondence to:
T. A. Middleton,
tim.middleton90@gmail.com

Citation:
Middleton, T. A., R. T. Walker, D. H. Rood, E. J. Rhodes, B. Parsons, Q. Lei, J. R. Elliott, Z. Ren, and Y. Zhou (2016), The tectonics of the western Ordos Plateau, Ningxia, China: Slip rates on the Luoshan and East Helanshan Faults, *Tectonics*, *35*, 2754–2777, doi:10.1002/2016TC004230.

Received 9 MAY 2016
Accepted 27 OCT 2016
Accepted article online 1 NOV 2016
Published online 29 NOV 2016

Abstract Analysis of the locus, style, and rate of faulting is fundamental to understanding the kinematics of continental deformation. The Ordos Plateau lies to the northeast of Tibet, within the India-Eurasia collision zone. Previous studies have suggested that it behaves rigidly and rotates anticlockwise within a large-scale zone of ENE-WSW left-lateral shearing. For this rotation to be accommodated, the eastern and western margins of the Ordos Plateau should be undergoing right-lateral shearing and yet the dominant faulting style appears to be extensional. We focus specifically on the kinematics of the faults bounding the western margin of the Ordos Plateau and make new slip rate estimates for two of the major faults in the region: the right-lateral strike-slip Luoshan Fault and the normal-slip East Helanshan Fault. We use a combination of infrared stimulated luminescence dating of offset landforms with high-resolution imagery and topography from the Pleiades satellites to determine an average right-lateral slip rate of 4.3 ± 0.4 mm/a (1σ uncertainty) on the Luoshan Fault. Similarly, we use ^{10}Be exposure dating to determine a vertical throw rate on the East Helanshan Fault of <0.6 ± 0.1 mm/a, corresponding to an extension rate of <0.7 ± 0.1 mm/a (1σ uncertainty). Both of these results agree well with slip rates determined from the latest campaign GPS data. We therefore conclude that right-lateral shearing is the dominant motion occurring in the western Ordos region, supporting a kinematic model of large-scale anticlockwise rotation of the whole Ordos Plateau.

1. Introduction

Deformation on the continents tends to be distributed across broad networks of faults [*Thatcher*, 2009]. For instance, in the India-Eurasia collision zone, 40 mm/a of relative motion is accommodated in a region spanning thousands of kilometers [*DeMets et al.*, 1990, 1994; *England and Molnar*, 1997; *Wang et al.*, 2001]. Within the India-Eurasia collision zone, though, there are also regions that appear not to deform. It is important to understand the active tectonics of such regions because nondeforming blocks tend to localize strain, and hence seismic hazard, at their margins [*Molnar and Dayem*, 2010], yet the style of faulting and rates of motion of these blocks are not always predictable from nearby plate velocities [*McKenzie and Jackson*, 1983; *Jackson and McKenzie*, 1988]. For example, large-scale transtensional shearing can sometimes be accommodated purely by en echelon normal faulting and vertical axis rotations of intervening crustal blocks [*Wesnousky et al.*, 2012].

The Ordos Plateau, which lies to the northeast of the Tibetan Plateau in northern central China, is one such apparently nondeforming region. It sits within the India-Eurasia collision zone—hence in a region of overall north-south shortening—and yet large normal faults and extensional grabens are present along most of its boundaries, suggesting that the region is extending in all directions (see Figure 1). Furthermore, both geological and GPS measurements indicate that the Ordos Plateau is situated within a large, left-lateral shear zone (see Figure 1). The cause of the Cenozoic extensional and strike-slip deformation in eastern Asia is debated, although it is likely to be some combination of lateral extrusion as India collides with Eurasia, gravitational collapse of the elevated Tibetan Plateau, and back-arc extension behind the subducting Philippine Sea Plate [e.g., *Tapponnier and Molnar*, 1976; *Northrup et al.*, 1995; *Liu et al.*, 2004; *Schellart and Lister*, 2005].

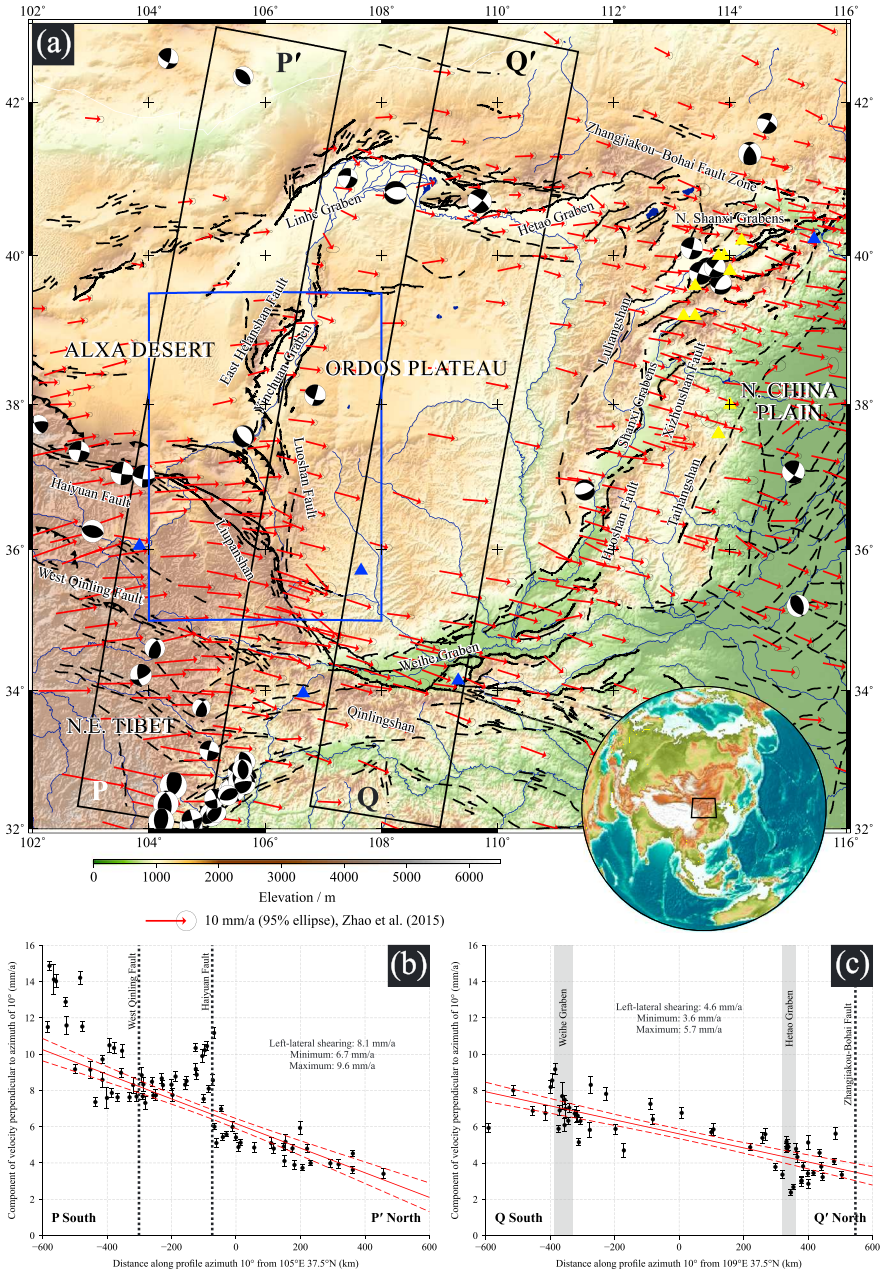

Figure 1. (a) Shuttle Radar Topography Mission (SRTM) topography of the Ordos Plateau in northeastern China [*Farr et al.*, 2007]. Focal mechanisms from the global centroid moment tensor (CMT) catalogue [*Ekström et al.*, 2012] are shown for recent earthquakes (1976 to present) with magnitudes greater than M_w 5.0. Red arrows show campaign GPS measurements made over a period of 4 years (occupations in 2009, 2011, and 2013) from *Zhao et al.* [2015] relative to stable Eurasia. Faults, marked as thin black lines, have been mapped from satellite imagery (source: http://earth.google.com) based upon earlier fault maps from *Tapponnier and Molnar* [1977], *Deng et al.* [1984], *Zhang et al.* [1986], *Zhang et al.* [1990], *Xu and Ma* [1992], *Deng and Liao* [1996], *Darby and Ritts* [2002], *Yu* [2004], and *Darby et al.* [2005]. Faults that are inferred or show no clear evidence of Quaternary activity are marked by dashed lines. Yellow triangles show locations of paleomagnetism samples used by *Xu et al.* [1994]; blue triangles show locations of paleomagnetism samples used by *Li et al.* [2001]. Rivers are indicated in dark blue. The blue polygon indicates the region shown in Figure 2. (b) Swath profile P-P′ through the GPS data west of the Ordos Plateau showing the velocity component perpendicular to the profile. The red line is the best fit least squares regression to the data, and the dashed red lines are the 95% confidence envelopes on this best fit line. The profile shows left-lateral shear of 8.1 ± 1.5 mm/a averaged over the extent of the profile—with approximately 5 mm/a being taken up on the Haiyuan Fault. (c) Same as Figure 1b but for swath profile Q-Q′ through the center of the Ordos Plateau, showing left-lateral shear of 4.6 ± 1.1 mm/a averaged over the extent of the profile—though it does not appear to be localized on any one individual structure. The difference between the two profiles is potentially due to absorption of some of the eastward motion in the Liupanshan thrust belt.

In this paper, however, we are concerned with the kinematics rather than the dynamics of deformation. One implication of the observed WNW-ESE left-lateral shearing is that the Ordos Plateau should be rotating anticlockwise about a vertical axis within this zone [*Xu and Ma*, 1992; *Xu et al.*, 1993; *Avouac and Tapponnier*, 1993; *Xu et al.*, 1994; *Zhang et al.*, 1995; *Peltzer and Saucier*, 1996; *Zhang et al.*, 1998; *Zhao et al.*, 2015]. Yet evidence for anticlockwise rotation of the Ordos Plateau is relatively sparse. *Xu et al.* [1994] used paleomagnetic data to estimate a total anticlockwise rotation of 1.3 to 3.7° with respect to the Xinjiang region of northwest China since the late Tertiary, corresponding to a rotation rate of 0.5 to 1.4°/Ma. However, their samples were from the deforming eastern margin of the Ordos Plateau (see Figure 1) and so are likely to be affected by local rotations within this deforming belt. Furthermore, *Li et al.* [2001] reported much higher anticlockwise rotation rates of tens of degrees per million years, also on the basis of paleomagnetic data (see Figure 1)—although their samples were also primarily from the deforming margins of the Ordos Plateau. *Fan and Ma* [2003] used the fairly sparse GPS data set of *Wang et al.* [2001] (including only six sites on the Ordos Plateau) to estimate an anticlockwise rotation rate of 0.02°/Ma about a pole at 51.5°N, 120.1°E with respect to stable Eurasia.

If anticlockwise rotation about a vertical axis really is important for the kinematics of the Ordos Plateau, we would expect to see dominantly right-lateral motion on both the eastern and western sides of the plateau as it rotates with respect to the Alxa Desert in the west and the North China Plain in the east (see Figure 1). On the eastern side of the Ordos Plateau it is known that right-lateral shearing occurs through normal faulting on the en echelon Shanxi Grabens and right-lateral slip on the Xizhoushan Fault (at 5.7 mm/a) and the Huoshan Fault (at 5.0 mm/a) [*Xu et al.*, 1986; *Xu and Deng*, 1990; *Xu et al.*, 1993]. On the western side of the Ordos Plateau, right-lateral faults are also identified, though their rates of motion and relative importance are debated [*Deng et al.*, 1984; *Min et al.*, 1992, 1993; *Zhang et al.*, 1998; *Min et al.*, 2003].

In this study we therefore examine the relative importance of right-lateral and extensional slip in the western Ordos region by determining Holocene rates for two of the major faults within the region: the Luoshan Fault (right-lateral strike slip) and the East Helanshan Fault (normal). We then consider our results within the context of a kinematic model of the Ordos Plateau that incorporates both anticlockwise rotation and the widespread normal faulting. Full details of all our methodologies—including construction of high-resolution Pleiades digital elevation models (DEMs) [*Smith and Wessel*, 1990; *Parsons et al.*, 2014; *Zhou et al.*, 2015], vertical and horizontal offset measurements [*Scharer et al.*, 2014; *Elliott et al.*, 2015], infrared stimulated luminescence (IRSL) dating [*Huntley et al.*, 1985; *Hütt et al.*, 1988; *Lamothe et al.*, 1994; *Murray and Wintle*, 2000; *Buylaert et al.*, 2009; *Rhodes*, 2011; *Lawson et al.*, 2012; *Neudorf et al.*, 2012; *Reimann et al.*, 2012; *Smedley et al.*, 2012; *Trauerstein et al.*, 2014; *Rhodes*, 2015; *Smedley et al.*, 2015], and ^{10}Be exposure dating [*Gosse and Phillips*, 2001; *Nishiizumi et al.*, 2007; *Xu et al.*, 2010; *Schmidt et al.*, 2011; *Benedetti and van der Woerd*, 2014; *Granger and Schaller*, 2014]—can be found online in the supporting information.

2. Tectonic Setting

The western Ordos region straddles the transition from shortening occurring in the northeastern corner of the Tibetan Plateau to extension occurring across the Yinchuan Graben (see Figure 2). The left-lateral Haiyuan Fault, with a Quaternary slip rate in the range of 5 to 10 mm/a [*Zhang et al.*, 1990; *Min et al.*, 2000; *Li et al.*, 2009], runs along the northeastern edge of the Tibetan Plateau and enters the southern part of Ningxia Province, on the western side of the Ordos Plateau, striking northwest-southeast and terminating in a series of reverse faults. These reverse faults form a south trending fold-and-thrust zone that extends as far as the Liupanshan at the southernmost extent of the province [*Deng et al.*, 1984; *Li et al.*, 2013]. The *M* 7.8 1920 left-lateral strike-slip-faulting Haiyuan earthquake occurred on the easternmost part of the Haiyuan Fault [*Zhang et al.*, 1987, 1988; *Burchfiel et al.*, 1991; *Lasserre et al.*, 2002; *Liu-Zeng et al.*, 2007; *Ren et al.*, 2015].

To the north of the Haiyuan Fault are two more oblique reverse faults: the Tianjinshan-Miboshan Fault (also called the Zhongwei-Tongxin Fault) and the Yantongshan Fault (see Figure 2). The existence and orientation of these ranges imply northeast-southwest crustal shortening, which is in agreement with modern GPS studies [*Gan et al.*, 2007; *Li et al.*, 2013]. The *M* 7.5 1709 oblique left-lateral strike-slip-faulting Zhongwei earthquake is thought to have occurred on the Tianjinshan-Miboshan Fault [*Nie and Lin*, 1993; *Min et al.*, 2001]. Meanwhile, the Luoshan Fault lies to the east of the Yantongshan Fault and the Niushoushan Fault to the north (see Figure 2). The *M* 7.3 1561 earthquake occurred near the Luoshan Fault [*Min et al.*, 2003], and recent work on the Niushoushan Fault suggests a late Quaternary right-lateral slip rate of ≈0.4 mm/a [*Lei et al.*, 2016].

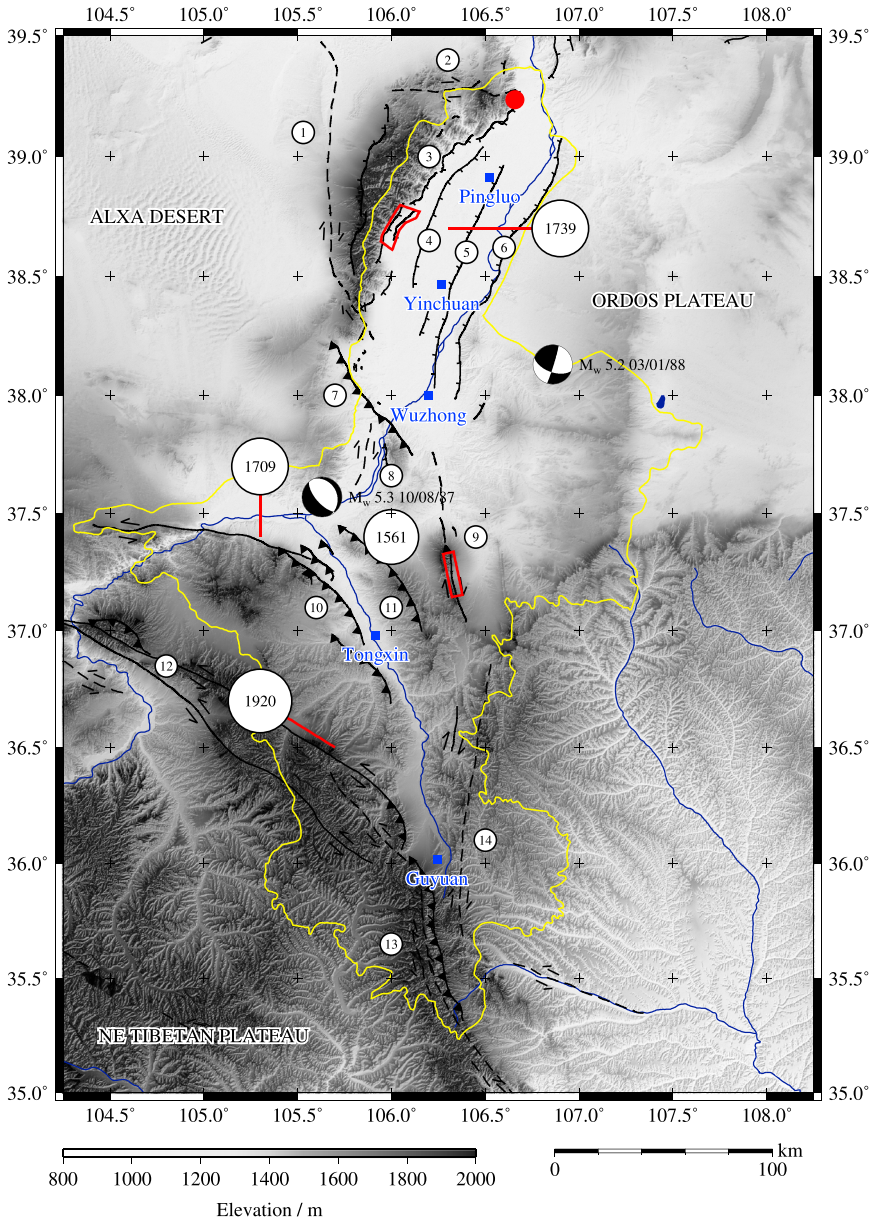

Figure 2. SRTM topography (30 m resolution) of the study area in the western Ordos region, Ningxia Province, northern China [*Farr et al.*, 2007]. The province is outlined in yellow, and cities are marked by blue squares. Focal mechanisms are from the global CMT catalogue [*Ekström et al.*, 2012]. Major historical earthquakes are shown by white circles, including the year in which they occurred [*Liu et al.*, 2011]. Red outlines indicate coverage of Pleiades data. Red circle indicates field site at the northern end of the East Helanshan Fault (see Figure 11). Faults are drawn as in Figure 1. Faults are numbered as follows: 1, Alxa Desert Fault; 2, Zhengyiguan Fault; 3, East Helanshan Fault; 4, Luhuatai Fault; 5, Yinchuan-Pingluo Fault; 6, Yellow River (Huang He) Fault; 7, Niushoushan Fault; 8, Baima Fault; 9, Luoshan Fault; 10, Tianjinshan-Miboshan (Zhongwei-Tongxin) Fault; 11, Yantongshan Fault; 12, Haiyuan Fault; 13, Liupanshan Fault; and 14, Yunwushan Fault.

The Yinchuan Graben is sited at the northern end of Ningxia Province, where the deformation appears to be markedly different. Four major northeast-southwest trending normal faults cut Cenozoic and Quaternary strata, accommodating apparently northwest-southeast extension. From west to east these faults are the following: the East Helanshan Fault, the Luhuatai Fault, the Yinchuan-Pingluo Fault, and the Yellow River Fault (see Figure 2). To the west of the Helanshan is another normal fault, but very little is known about its kinematics or rate of motion [*Deng et al.*, 1984; *Zhang et al.*, 1990]. The *M* 7.6 1739 normal-faulting Yinchuan earthquake ruptured the East Helanshan Fault [*Liao and Pan*, 1982; *Zhang et al.*, 1986; *Deng and Liao*, 1996; *Lei et al.*, 2015; *Middleton et al.*, 2016].

3. The Luoshan Fault

3.1. Background

The Luoshan Fault is approximately 60 km long and runs along the eastern side of the Luoshan (Luo Mountains) [*Min et al.*, 2003]. The Luoshan comprises two ranges: the Daluoshan (Big Luo Mountains) to the north and the Xiaoluoshan (Small Luo Mountains) to the south, both of which are composed of Ordovician basement (see Figure 3). The Luoshan Fault was originally thought to be a left-lateral strike-slip fault [*The Research Group on Active Fault System around Ordos Massif*, 1988; *Zhang et al.*, 1990; *Zhou et al.*, 2000], but a detailed reassessment found numerous examples of right-lateral offsets in Quaternary and Holocene material [*Min et al.*, 1992, 1993, 2003]. Evidence for recent, right-lateral motion is also seen farther south on the Yunwushan Fault in the form of displaced river channels (for example, at 36.635°N, 106.349°E and 36.531°N, 106.333°E—see Figure 2). The finite slip on the Luoshan Fault is not known. *Min et al.* [2003] used two thermoluminescence (TL) ages to estimate a minimum, right-lateral slip rate on the Luoshan Fault since the late Pleistocene of 2.15 ± 0.20 mm/a, and the fault is assigned a right-lateral rate of 3 mm/a on the *Map of Active Tectonics in China* [*Deng et al.*, 2007]. *Min et al.* [2003] also suggested that the *M* 7.3 1561 earthquake occurred on the Luoshan Fault (see Figure 2) on the basis that comparatively young looking gullies (1 m deep) record offsets of 1.5 to 5.4 m and that a free face is visible on some scarps, particularly near the village of Zhangjiashanpo (see Figure 3a for location). Given the uncertainty about the kinematics of the Luoshan Fault and the paucity of slip rate constraints, we revisit the fault in this study using up-to-date luminescence methods and modern satellite imagery.

At its northern end, the Luoshan Fault strikes at 353° and runs along the eastern side of the Luoshan mountains just west of Tanzhuangzicun (see Figure 3). Gullies draining these mountains dissect an alluvial apron, draining first to the east and then curving to the north to follow the local slope, and preserve evidence of right-lateral offsets. Moving south, the fault strike changes to 330° around the northern end of the Daluoshan. Surface offsets are harder to identify, but *Min et al.* [2003] found evidence of thrusting in this section. The fault then tracks south, with a strike of 358°, cutting across at least four different generations of alluvial fans (F1 to F4, where F1 is the youngest and F4 is the oldest) emanating from the Daluoshan. The older fans are more heavily incised, and the channels on these surfaces are more sinuous. Multiple, parallel scarps are seen in this section, most of which include a component of uplift on their western side; the youngest fans preserve a vertical offset of 1.1 ± 0.3 m. At the southern end of the Daluoshan section, the fault makes a small dog-leg to the southeast and forms a 5 to 10 m high, 500 m long pressure ridge at 37.240°N, 106.322°E.

Moving south again, the fault lies along the eastern side of the Xiaoluoshan with a strike of 342°. It cuts across the heads of a number of alluvial fans, most of which appear to be of the same age on the basis of their color and texture (for example, see Figure 4). The streams draining the Xiaoluoshan preserve a number of examples of right-lateral offsets, and the fans here are uplifted on the eastern side of the fault trace by 5.0 ± 1.4 m (see Figure 4a). The fault then continues in this orientation until the southern end of the Xiaoluoshan, 9 km south of Zhangjiashanpo. In addition, a series of 12 to 23 m high east facing scarps are present east of the main strike-slip fault, between 106.34°E and 106.39°E (see Figure 3). We interpret these scarps to represent superficial spatial separation of strike-slip and reverse components of motion onto two parallel fault strands.

The smallest vertical offset (1.1 ± 0.3 m), at 37.255°N, 106.320°E, was measured where the local fault strike was 003°. Other sections of the fault, with more northwesterly strikes, showed larger vertical offsets indicating a greater amount of shortening. We therefore deduce that pure strike-slip motion occurs at an azimuth slightly east of 003°.

3.2. Xiaoluoshan Section

3.2.1. Overview and Offset Measurement

Our first slip rate site on the Luoshan Fault was adjacent to the Xiaoluoshan (see Figure 3a). Here the fault cuts through an alluvial apron on the eastern side of the mountains, and a large number of channels (approximately 300 m spacing) flow eastward across the fault trace, draining the Xiaoluoshan. Almost all of these channels show evidence of tens of meters of right-lateral offset. There is also a small amount of uplift (5.0 ± 1.4 m) on the eastern side of the fault trace (see Figure 4a).

Given that the whole area appears to be covered by an alluvial apron composed of coalesced fans of the same age, we propose that all of the geomorphological markers should preserve the same offset. We measured the horizontal offsets preserved by nine different markers (six channel riser tops, one channel riser bottom,

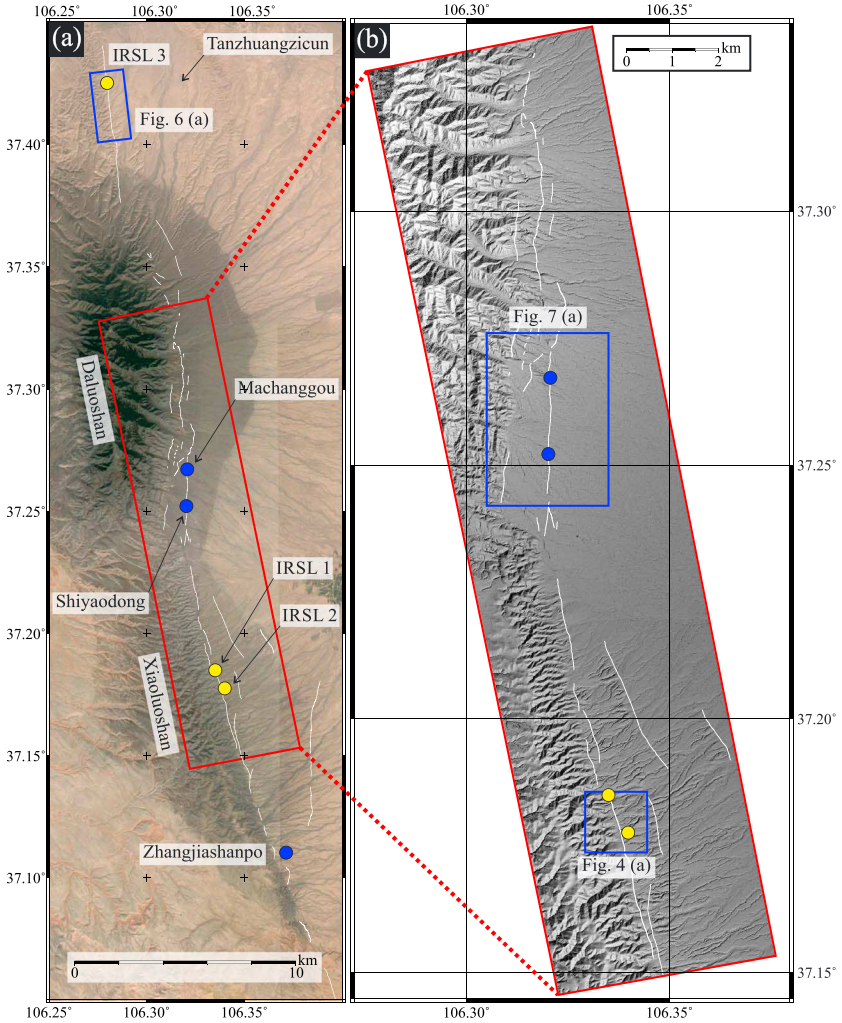

Figure 3. (a) Google Earth imagery from April and December 2013 (source: http://earth.google. com) of the Luoshan Fault with fault scarps mapped in white. Slip rate sites in this study are marked by yellow dots; sites from *Min et al.* [2003] are marked by blue dots. Red polygon shows coverage of Pleiades data. (b) Pleiades DEM of the central portion of the Luoshan Fault. Blue polygons show locations of other figures.

and two channel thalwegs—see yellow lines in Figure 4b) and obtained a mean offset of 37.2 ± 5.5 m and a range of 29.2 to 44.4 m (see supporting information). At the site of IRSL sample 1, the right-lateral fault motion is superposed on a preexisting channel meander so the horizontal offset is hard to determine. However, Figures 4c and 4d show that a 37 m restoration aligns both a channel thalweg to the south of the sampling site and a ridge crest adjacent to the site. At the site of IRSL sample 2, Figures 4e and 4f show that the 37 m restoration aligns an indistinct riser on the western side of the fault trace with a more pronounced channel margin on the uplifted eastern side.

3.2.2. Age Constraints and Slip Rate

IRSL sample 1 was taken from an alluvial surface on the eastern side of the fault at 37.185°N, 106.335°E. The sample was from a fine-grained, brown loess 1.5 m below the ground surface. However, due to erosion at the site, this was estimated in the field to correspond to 2.1 m below the top of the adjacent alluvial fan. The sample was overlain by a coarser sand layer and at least two gravel layers with 5 cm, subangular clasts of dark, Paleozoic bedrock (see Figure 5b). The sample provided an age of 141 ± 12 ka (see Table 1).

IRSL sample 2 was taken from a channel riser, 930 m to the southeast of IRSL sample 1, at 37.178°N, 106.340°E. The sample was from a patch of slightly coarser sand interbedded with fine-grained, brown loess at a depth of 55 cm. An angular gravel layer with 10 cm clasts was visible approximately 30 cm above the sample

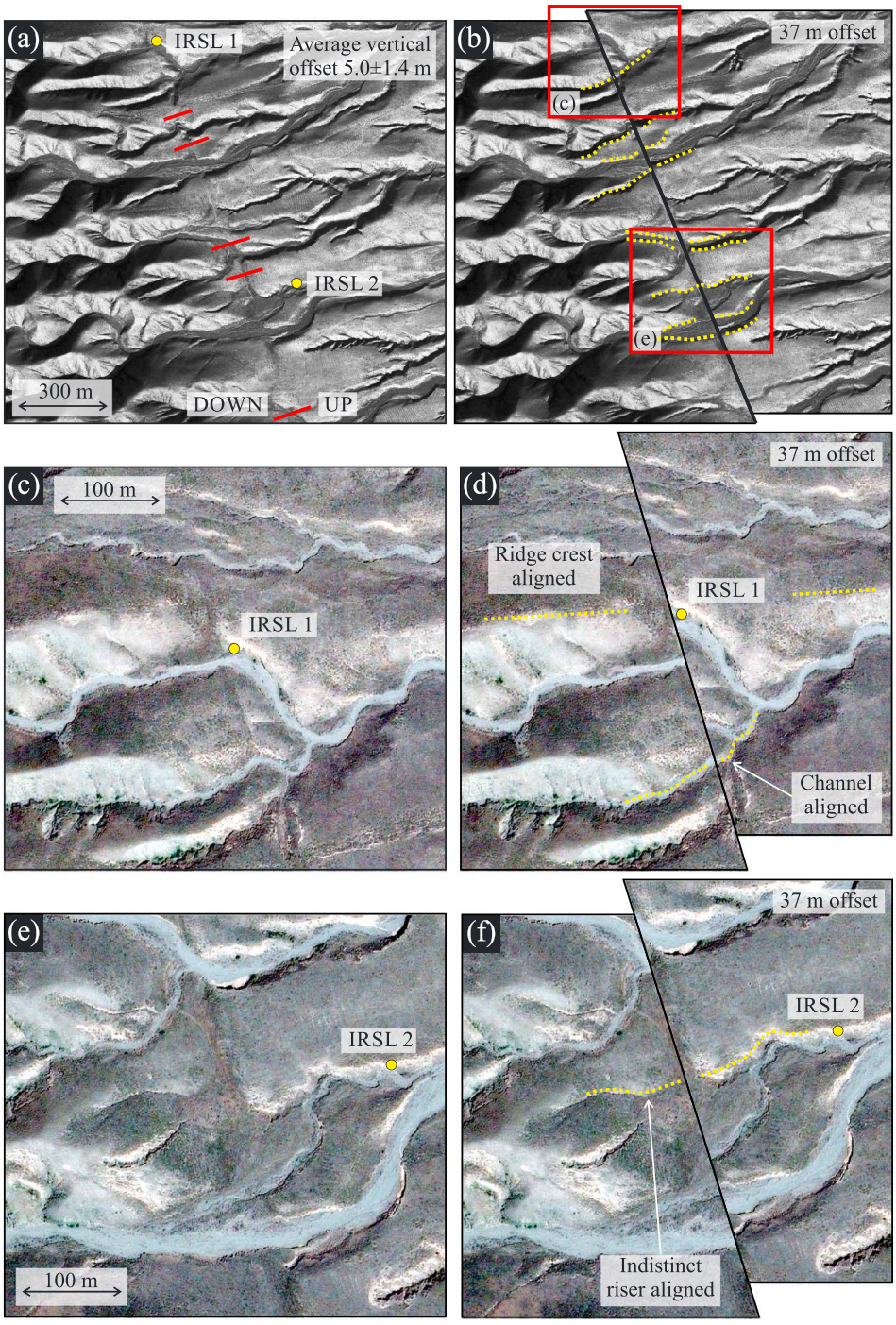

Figure 4. (a) 0.5 m resolution Worldview imagery showing a section of the Luoshan Fault adjacent to the Xiaoluoshan (see Figure 3 for precise location). The fault cuts across the image from NNW to SSE. As well as the strike-slip motion there is uplift on the eastern side of the fault trace. Red lines indicate locations of topographic profiles used to estimate the average vertical offset of 5.0 ± 1.4 m. The locations of IRSL samples 1 and 2 are indicated by yellow circles. (b) The 37 m restoration, aligning various channel thalwegs and terrace risers (highlighted in yellow). Red boxes indicate locations of figures below. (c) The 0.5 m resolution Pleiades imagery of the region marked in Figure 4b and showing the location of IRSL sample 1. (d) Same as Figure 4c with a 37 m restoration, aligning the channel thalweg to the south of the image and the ridge crest adjacent to the sampling site. (e) The 0.5 m resolution Pleiades imagery of the region marked in Figure 4b and showing the location of IRSL sample 2. (f) Same as Figure 4e with a 37 m restoration, aligning the sampled terrace riser.

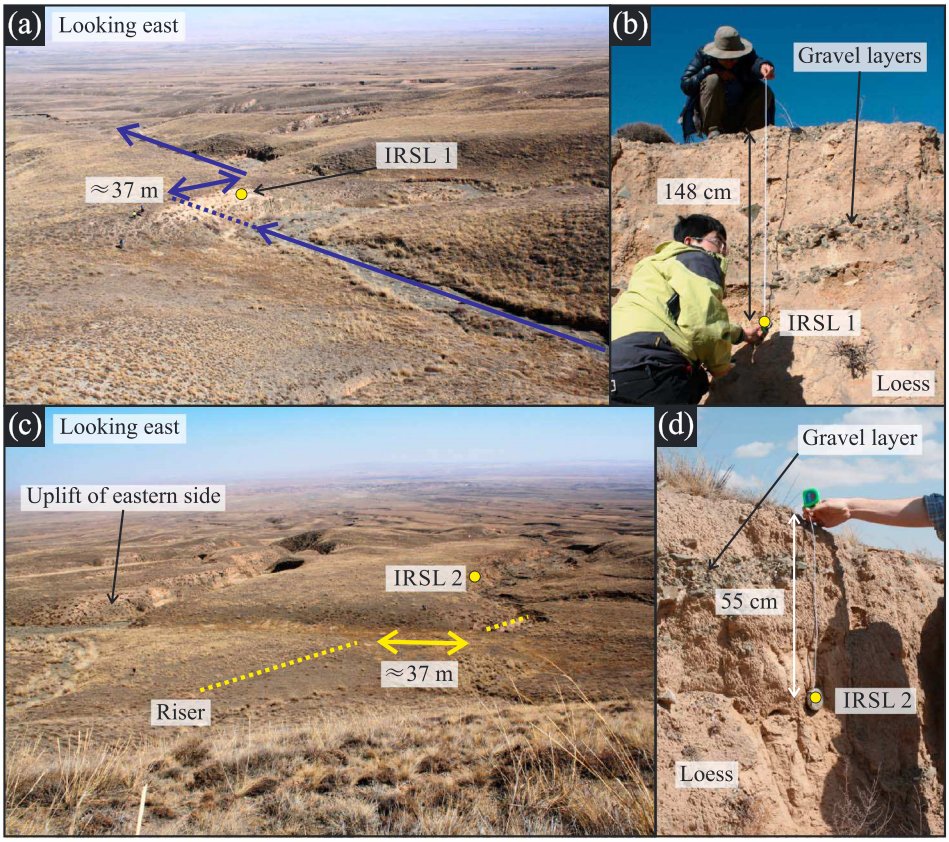

Figure 5. (a) Field photograph (taken at 37.185°N, 106.335°E) showing an overview of IRSL sample site 1. There is a large meander in the stream at the location of the fault trace, but the far-field offset is of the order of 37 m. (b) Close-up field photograph showing the sedimentary context of IRSL sample 1. (c) Field photograph (taken at 37.178°N, 106.340°E) showing an overview of IRSL sample site 2. A riser on the western side of the fault trace, highlighted in yellow, can be identified by a change in the grass cover. (d) Close-up field photograph showing the sedimentary context of IRSL sample 2.

(see Figure 5d), ensuring that we were dating material that was deposited prior to or during a fluvial regime, rather than aeolian deposits that accumulated after fan abandonment. The IRSL sample provided an age of 9.2 ± 0.6 ka (see Table 1).

The mean offset (37 m) and the age of IRSL sample 1 allow us to calculate a minimum slip rate of 0.26 ± 0.05 mm/a (see Table 2). Meanwhile, IRSL sample 2 indicates a minimum slip rate of 4.1 ± 0.7 mm/a (see Table 2). IRSL sample 1 is from deeper in the stratigraphy than IRSL sample 2 and may therefore represent sediments from a period of fan aggradation older than the most recent fan-forming episode. It is therefore unlikely to represent the age of the observed offset and can only be taken as a minimum age constraint. These slip rate results are discussed further in section 5.

Table 1. IRSL Dating Results

Location	Name	Latitude (deg)	Longitude (deg)	Elevation (m)	Depth (m)	Equivalent Dose[a] (Gy)	Dose Rate[a] (mGy a^{-1})	Age[a] (ka)
Xiaoluoshan Fault	1	106.3350	37.1850	1761	2.13	536 ± 39	3.80 ± 0.16	141 ± 12
Xiaoluoshan Fault	2	106.3397	37.1780	1766	0.55	33.0 ± 1.4	3.61 ± 0.16	9.16 ± 0.57
Daluoshan Fault	3	106.2800	37.4250	1422	1.69	39.6 ± 2.8	3.74 ± 0.16	10.6 ± 0.9
East Helanshan Fault	4	106.6575	39.2360	1374	0.54	5.25 ± 0.50	4.13 ± 0.19	1.27 ± 0.14
East Helanshan Fault	5	106.6575	39.2360	1374	1.27	16.0 ± 0.6	4.99 ± 0.25	3.21 ± 0.21

[a]Including 1σ analytical uncertainties.

Table 2. Calculated Slip Rates and Throw Rates

Location	Sample No.	Latitude (deg)	Longitude (deg)	Age (ka)	Error (ka)	Horizontal Offset (m)	Error (m)	Slip Rate (mm/a)	Error (mm/a)
				Luoshan Fault					
Xiaoluoshan	IRSL 1	37.1850	106.3350	141	12	37.2	5.5	>0.26	0.05
Xiaoluoshan	IRSL 2	37.1780	106.3397	9.16	0.57	37.2	5.5	4.1	0.7
Tanzhuangzicun	IRSL 3	37.4250	106.2800	10.6	0.9	50.6	6.7	4.8	0.8
Shiyaodong[a]	TL	37.2519	106.3204	9.80	0.75	41.1	5.9	4.2	0.7
Machanggou	TL	37.2672	106.3207	69.0	5.4	171	10	>2.5	0.2
Average[b]								**4.3**	**0.4**[c]
				East Helanshan Fault					
Northern end of fault	IRSL 4	39.2360	106.6575	1.27	0.14	16.0	5.0	12.6	4.2
Northern end of fault	IRSL 5	39.2360	106.6575	3.21	0.21	16.0	5.0	5.0	1.6
Location	Sample No.	Latitude (deg)	Longitude (deg)	Age (ka)	Error (ka)	Vertical Offset (m)	Error (m)	Throw Rate (mm/a)	Error (mm/a)
				East Helanshan Fault					
Suyukou scarps, T5	STM10[d]	38.7839	106.1343	221.5	3.9	19.4	1.1	0.09	0.01
Suyukou scarps, T5	STM10[e]	38.7839	106.1343	157.2	4.1	19.4	1.1	0.12	0.01
Helanshan range front	STM9[d]	38.7359	106.0117	120.6	1.9	24.0	4.0	0.20	0.03
Helanshan range front	STM9[e]	38.7359	106.0117	56.3	2.2	24.0	4.0	0.43	0.07
Sum[f]								**<0.6**	**0.1**
Extension rate[g]								**<0.7**	**0.1**

[a]Reassessment of the data from Shiyaodong [*Min et al.*, 2003].
[b]Error-weighted average of samples IRSL 2, IRSL 3, and TL from Shiyaodong.
[c]Error is the weighted standard deviation of the three slip rate estimates.
[d]Assuming a zero inheritance model.
[e]Corrected for inheritance by subtracting STM13A.
[f]Sum of 0.12 and 0.43 mm/a for parallel Suyukou and range front strands.
[g]Assuming fault dip of 39° from *Fang et al.* [2009].

3.3. Tanzhuangzicun Section

3.3.1. Overview and Offset Measurement

Our second slip rate site on the Luoshan Fault was at its northern end, beyond the end of the Daluoshan and around 1.75 km west of the village of Tanzhuangzicun (see Figure 3a). This section of the fault strikes at 355° and cuts across an alluvial apron into which a number of channels have been incised (see Figure 6a). The alluvial surface itself has been modified and terraced for agriculture (see Figures 6b and 6c), and some very young streams have developed on top of this modified surface. However, evidence for right-lateral fault motion has been preserved by the channel margins of the more heavily incised streams. The whole fan surface slopes gently to the north, and so the channels are offset in the opposite direction to the regional gradient. We also saw evidence of eroded corners of channel risers on the downslope edges of the channels (see Figures 6d and 6e) [e.g., *Cowgill*, 2007].

The mean offset recorded by 10 different geomorphological markers (eight channel riser tops, one channel riser bottom, and one channel thalweg) on this single alluvial surface was 50.6 ± 6.7 m with a range of 37.2 to 61.4 m (see supporting information). Figures 6d and 6e show how a 51 m restoration achieves reasonable alignment of all of these markers, including those immediately adjacent to the site of IRSL sample 3.

3.3.2. Age Constraints and Slip Rate

IRSL sample 3 was taken at 37.425°N, 106.280°E, just to the east of the fault trace. The sample was from fairly homogeneous, fine, yellow-brown loess, 169 cm below the ground surface and approximately 15 cm below a thin gravel layer with 5 cm clasts of angular material (see Figure 6g). The sample provided an age of 10.6 ± 0.9 ka (see Table 1). The mean offset (51 m) and the age of IRSL sample 3 allow us to calculate a minimum slip rate along the Tanzhuangzicun section of 4.8 ± 0.8 mm/a (see Table 2).

3.4. Shiyaodong Site

3.4.1. Overview and Offset Measurement

Min et al. [2003] used TL dates from two sites (Shiyaodong and Machanggou) at the southern end of the Daluoshan section to obtain their slip rate estimate of 2.15 ± 0.20 mm/a (see Figure 3). Here we

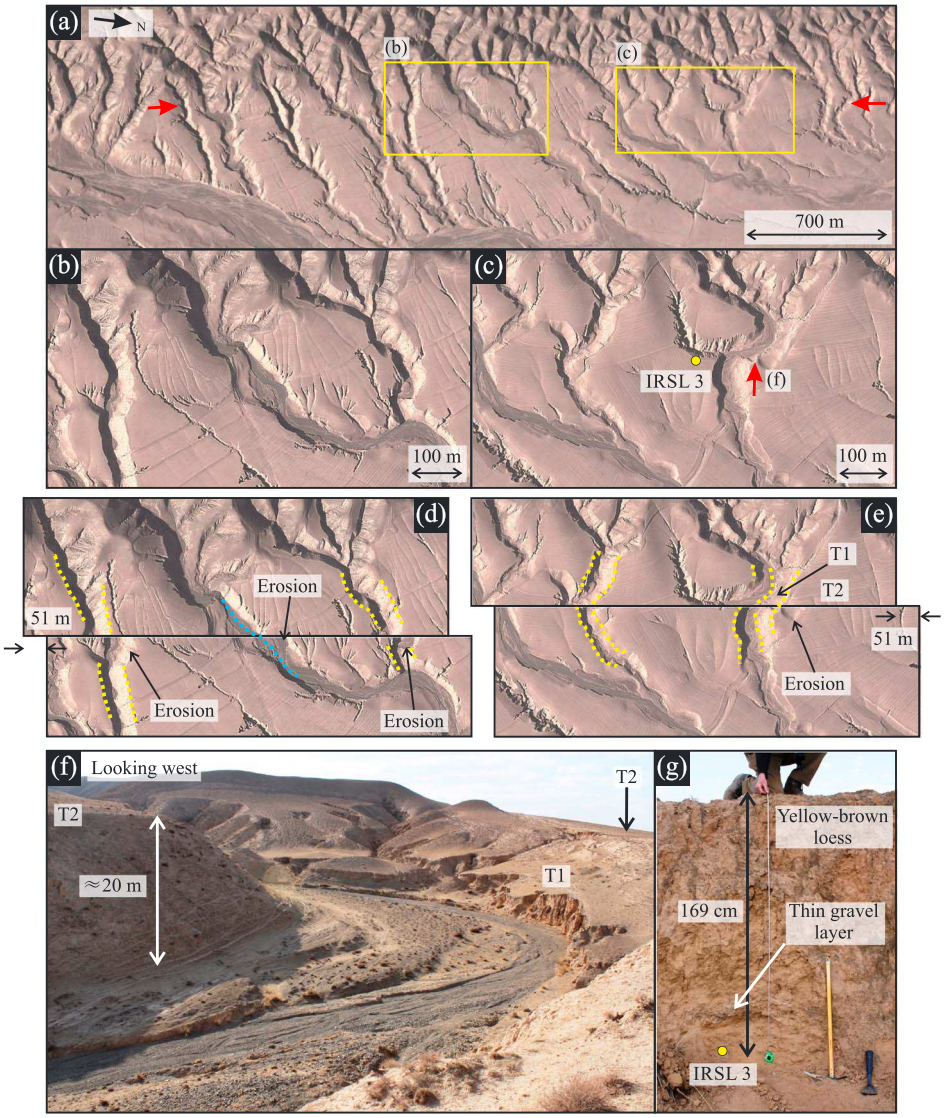

Figure 6. (a) Google Earth imagery from December 2013 (source: http://earth.google.com) of the Luoshan Fault north of the Daluoshan and around 1.75 km west of the village of Tanzhuangzicun (see Figure 3a for precise location). Fault location is marked by red arrows. (b) Zoomed in view of the Google Earth imagery at the location marked in Figure 6a. (c) Zoomed in view of the Google Earth imagery at the location marked in Figure 6a. The location of IRSL sample 3 (at 37.425°N, 106.280°E) is indicated by the yellow circle. (d) Restoration of Figure 6b indicating 51 m of right-lateral offset. Aligned channel risers are highlighted in yellow, and an aligned channel thalweg is shown in blue. Eroded corners of channel margins on downslope (i.e., northern) side are also indicated. (e) Restoration of Figure 6c indicating 51 m of right-lateral offset. Yellow lines highlight alignment of two channel risers. (f) Field photograph taken at the location indicated in Figure 6c showing the two terrace levels adjacent to this channel. (g) Field photograph showing the sedimentary context of IRSL sample 3.

use the high-resolution Pleiades DEM, slope and roughness maps, and our geomorphological mapping to reassess their sites.

At the southern end of the Daluoshan section, four different generations of alluvial fans can be identified on the basis of their surface texture and degree of incision (see Figure 7). The Shiyaodong site is on the F3 surface, and *Min et al.* [2003] measured an offset of 18 ± 1 m. However, although an 18 m restoration at this site realigns nearby gullies on F1, it does not appear to realign the gullies on F3 (see Figure 7e). The restoration is also complicated by the fact that the channels on the F3 surface are highly sinuous, leading to a large degree of ambiguity in the amount of slip. However, we remeasured the horizontal offsets of five piercing lines for

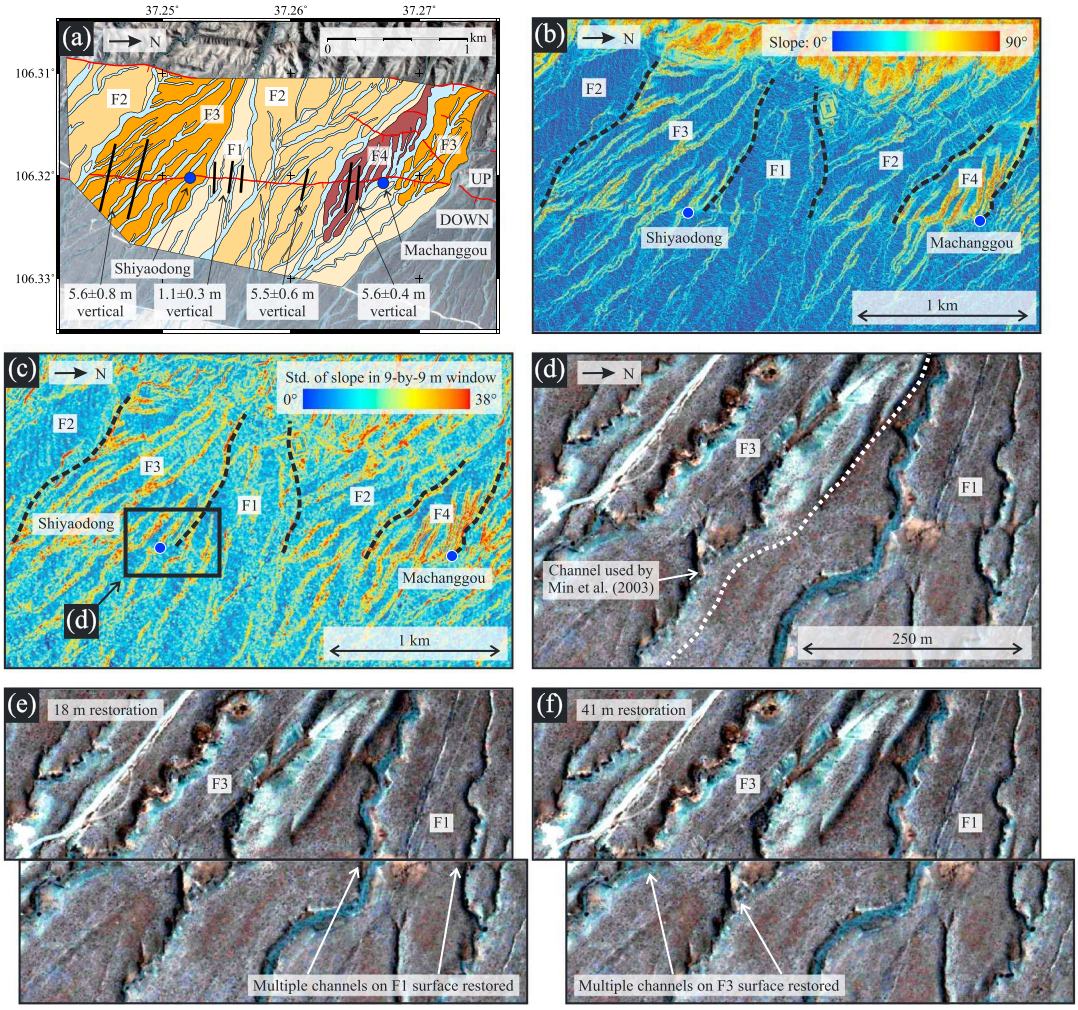

Figure 7. (a) Pleiades imagery in the vicinity of the slip rate sites used by *Min et al.* [2003]. Alluvial surfaces of different ages are shown in different shades of brown, and fault scarps, running north-south, are mapped in red. Black lines indicate the locations of topographic profiles used to estimate the vertical offset preserved by each fan surface (western side uplifted). (b) Slope map derived from the Pleiades DEM. Region covered is roughly the same as in Figure 7a. Blue circles show the locations of the slip rate sites used by *Min et al.* [2003]. (c) Surface roughness map of the same area derived from the Pleiades DEM by taking the standard deviation of the slope of the DEM in a 9×9 m moving window [*Frankel and Dolan*, 2007]. (d) Pleiades imagery of the Shiyaodong site from *Min et al.* [2003] indicating the gully used for their slip rate estimate at the edge of the F3 surface. (e) The 18 m reconstruction, showing that gullies on the F1 surface are restored, but not those on the F3 surface. (f) The 41 m reconstruction, which properly aligns gullies on the F3 surface.

channel thalwegs incised into the F3 surface and obtained a mean offset of 41.1 ± 5.9 m and range of 33.8 to 48.5 m (see supporting information and Figure 7f).

3.4.2. Age Constraints and Slip Rate

At Shiyaodong (37.252°N, 106.320°E) *Min et al.* [2003] obtained a TL age of 9.80 ± 0.75 ka for the F3 surface. Using our new offset measurement, we therefore estimate a new slip rate of 4.2 ± 0.7 mm/a (see Table 2).

3.5. Machanggou Site

3.5.1. Overview and Offset Measurement

At the Machanggou site, 1.7 km north of Shiyaodong (see Figure 3), *Min et al.* [2003] measured an offset of 171 ± 10 m. However, according to our geomorphological mapping (see Figure 7a), the channel *Min et al.* [2003] investigated runs along the side of the F4 surface rather than being incised into it. Their measured offset may therefore not be representative of the displacement recorded by F4.

3.5.2. Age Constraints and Slip Rate

At Machanggou (37.267°N, 106.321°E), *Min et al.* [2003] obtained a TL age of 69.0 ± 5.4 ka. However, their sample was from 3 m below the surface of F4 and so may well be significantly older than that last episode

of deposition on this surface (as we interpreted for our IRSL sample 1). Due to the uncertainty in the offset measurement and age constraint at this site, we are only able to estimate a minimum slip rate of 2.5 ± 0.2 mm/a at Machanggou (see Table 2).

Furthermore, we measured similar vertical offsets for F2, F3, and F4 (see Figure 7a), suggesting that all three of these surfaces preserve the same fault activity. The abandonment of these fan surfaces is likely to have been climatically controlled, and hence, the best constraint on the slip rate at this site would be provided by dating the youngest of these fans (F2). The F4 surface is probably notably older than the initiation of scarp formation at this site, and the slip rate from *Min et al.* [2003], based on the age from F4, is therefore likely to be a significant underestimate. Hence, we are not able to improve upon the slip rate estimate from *Min et al.* [2003] and we do not include this result in our mean slip rate for the whole fault (see Table 2).

4. The East Helanshan Fault

4.1. Background

The East Helanshan Fault is approximately 120 km long and runs along the eastern side of the Helanshan (Helan mountains). It is not known exactly when normal displacement began on the East Helanshan Fault, but it is thought to have initiated since the Oligocene and the present-day cumulative vertical displacement could be more than 7 or 8 km [*Zhang et al.*, 1990]. *Zhang et al.* [1990] also used the 1 to 1.6 km thickness of Quaternary sediments in the basin to estimate a Quaternary throw rate for the East Helanshan Fault of 0.5 to 0.8 mm/a. The throw rate on the Yellow River Fault is estimated from TL ages of offset river terraces to be around 0.23 to 0.25 mm/a [*Liao et al.*, 2000]. Throw rates on the Yinchuan-Pingluo and Luhuatai are estimated from composite drilling profiles to be 0.14 mm/a (^{14}C date) and 0.18 mm/a (luminescence date), respectively [*Lei et al.*, 2008, 2011, 2015]. According to a cross-sectional area balance, the whole Yinchuan Graben is thought to have extended at 2.9 ± 1.0 mm/a since the Pliocene, though this result relies on the interpretation of seismic reflection profiles [*Zhang et al.*, 1998]. The graben also contains approximately 6 km of pre-Quaternary deposits [*Zhang et al.*, 1990].

A series of fresh scarps are present along the East Helanshan Fault [*Liao and Pan*, 1982]. The southernmost section of these scarps is called the Suyukou scarps, which vary in strike between 10 and 50° and cut through four, large, coalesced, alluvial fans some 3 km from the range front (see Figure 8). From south to north, these fans are called the Baisikou, Suyukou, Helankou, and Chaqikou Fans [*Deng and Liao*, 1996]. *Deng and Liao* [1996] also identified four separate terrace levels in the scarp footwalls, from T1 (the youngest, typically 3 m high and thought to be from the 1739 Yinchuan earthquake) to T4 (the oldest, up to 11 m high). The Baisikou, Suyukou, and Helankou Fans are mainly mantled by the T2 surface, with only scattered remnants of T3 and T4—although the T1 surface is found adjacent to currently active channels (T0). The Chaqikou Fan comprises primarily the T1 and T2 surfaces. Landforms older than T4 are only preserved in a few small areas. First, at the range front, some older terraces are preserved adjacent to minor catchments. Second, north of the Chaqikou Fan, there is a remnant of a heavily incised terrace (colored dark brown in Figure 8b), which is cut by multiple fault scarps and predates T4. We call this terrace T5.

On the basis of paleoseismic trenching and radiocarbon dating at the Suyukou scarps (and farther north on the East Helanshan Fault), *Deng and Liao* [1996] concluded that at least three earthquakes occurred on this fault prior to 1739: 2600 years ago, 4600–6300 years ago, and 8400 years ago. If these trench ages correlate with the terrace surfaces preserved in the alluvial fans, then the offsets measured on the terraces can be used to calculate a throw rate. *Deng and Liao* [1996] measure a combined terrace offset for the last three events of 8.4 m. Combined with an age for the antepenultimate event of 6300 years, this yields a throw rate of 1.3 mm/a. In this study, however, we seek to provide the first direct measurement of the late Quaternary throw rate on the East Helanshan Fault by conducting ^{10}Be dating of the older terrace surfaces and by making new vertical offset measurements from high-resolution topography.

4.2. T5 at the Northern End of the Suyukou Scarps

4.2.1. Overview and Offset Measurement

Our first throw rate site was on T5, at the northern end of the Suyukou scarps (see Figures 8 and 9). Multiple fault scarps cut T5, all of which must have formed since the abandonment of this surface. Topographic profiles from the Pleiades DEM show a combined offset across all of these scarps of 19.4 ± 1.1 m (see Figure 9 and the supporting information for methodology).

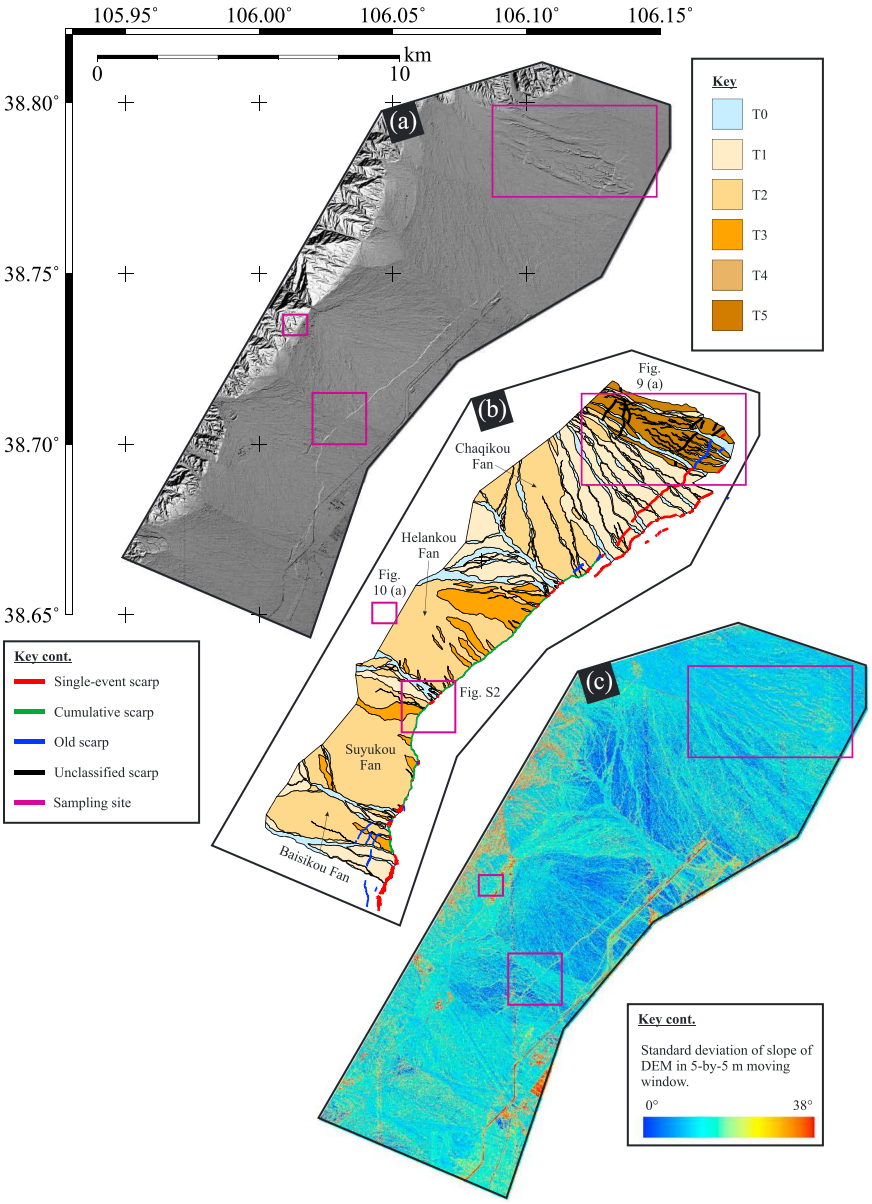

Figure 8. (a) Pleiades DEM for the Suyukou scarps at the southern end of the East Helanshan Fault. (b) Interpreted tectonic geomorphology for the Suyukou scarps at the southern end of the East Helanshan Fault. Purple polygons indicate the locations of ^{10}Be sampling sites, as shown in Figures 9a, 10a, and supporting information Figure S2. (c) Surface roughness map derived from the Pleiades DEM by taking the standard deviation of the slope of the DEM in a 5×5 m moving window [*Frankel and Dolan*, 2007].

4.2.2. Age Constraints and Throw Rate

A suite of eight quartz pebbles (samples 11A to 11H, from 38.783°N, 106.140°E) and an amalgamated sample of 53 smaller clasts (sample 10, from 38.784°N, 106.134°E) were taken for ^{10}Be dating from the surface of T5 (see Figure 9 and Table 3). Five of the eight clasts are in relatively close agreement with the aggregate age of 221.5 ± 3.9 ka. We therefore interpret the three younger clasts (samples 11A, 11D, and 11E) as outliers.

An amalgamated sample of 42 pebbles (sample 12) and two individual clasts (samples 13A and 13B) were taken from the modern river (at 38.777°N, 106.129°E; see Figure 9 for location) to estimate the inheritance in this particular system. We obtained ^{10}Be ages of 27.5 ± 0.7 ka for the amalgamated sample and 64.3 ± 1.2 ka and 8.0 ± 0.4 ka, respectively, for the two clasts. Although the small number of samples indicates a large range in the inherited component, and the seasonal nature of the modern river could mean that these samples

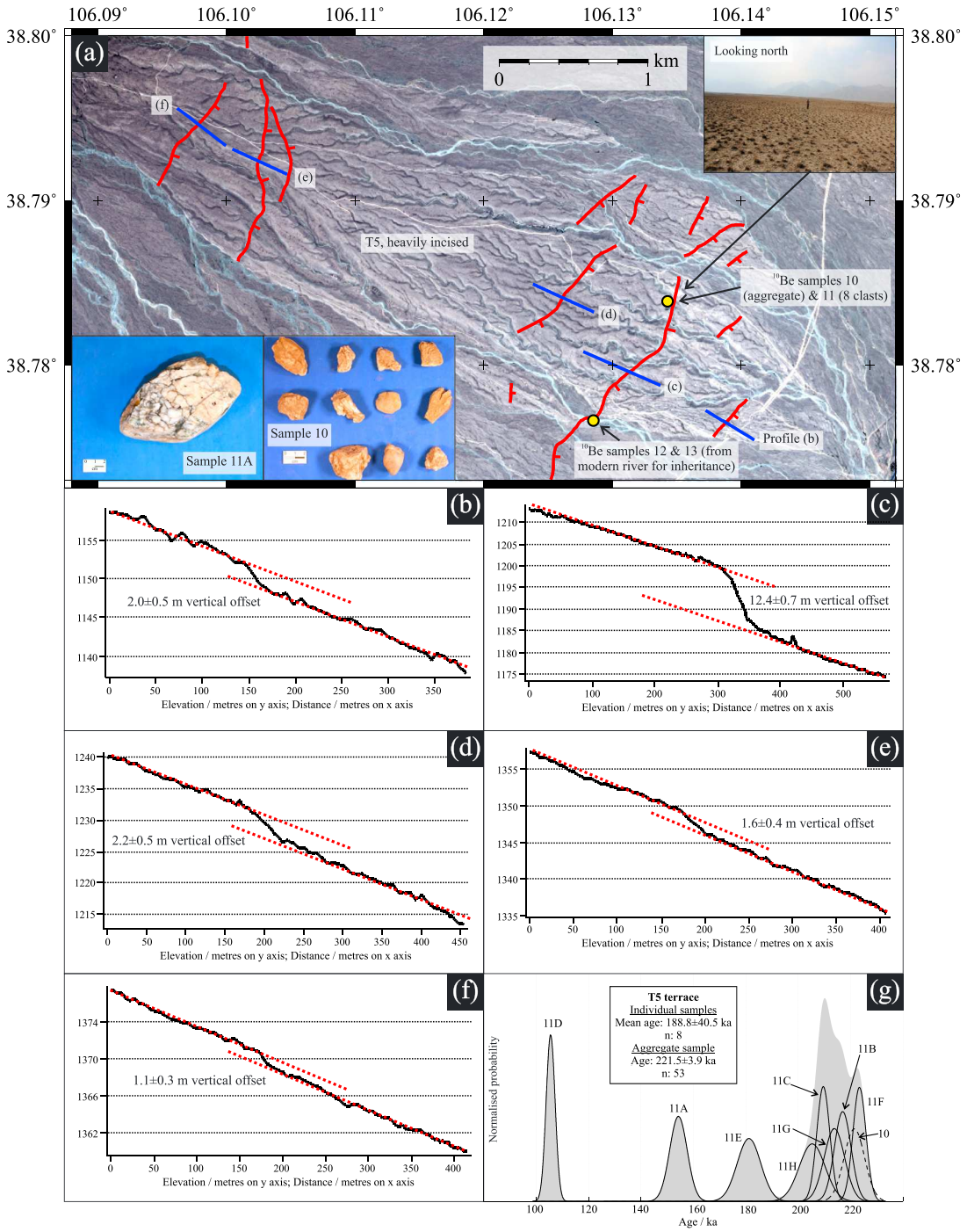

Figure 9. (a) Pleiades imagery showing the heavily incised T5 alluvial surface at the northern end of the Suyukou scarps. Fault traces are marked in red, and ^{10}Be sample locations are shown by yellow circles. Inset photographs show the T5 surface (taken at 38.784°N, 106.134°E) and some of the quartz pebbles collected from this surface for ^{10}Be dating. (b–f) Topographic profiles along the blue lines marked in Figure 9a. For each fault strand the vertical offset is labeled. The total offset of the T5 surface is hence 19.4 ± 1.1 m. (g) ^{10}Be age results for T5. The black curves are normally distributed probability density functions (PDFs) for individual samples, defined by their age and 1σ analytical error. The grey curve is a normal kernel density estimate (or camel plot), obtained by summing the individual PDFs. The dashed black curve is a normally distributed PDF for the aggregate sample.

Table 3. ^{10}Be Dating Results

Location	Name	Type[a]	Latitude (deg)	Longitude (deg)	Elevation (m)	Thickness (cm)	Density (g cm^{-3})	Shielding Factor	[^{10}Be][b] (10^3 atoms g^{-1})	Exposure Age[c] (ka)
Range front terrace	STM9	A	38.7359	106.0117	1461	2	2.7	0.9628	1498.0 ± 22.7	120.6 ± 1.9
Range front terrace	STM1	B	38.7363	106.0111	1486	3	2.7	0.9674	1409.0 ± 24.7	111.5 ± 2.0
Range front fan	STM3	B	38.7354	106.0143	1414	3	2.7	0.9832	206.2 ± 7.0	16.5 ± 0.6
Range front fan	STM4	B	38.7353	106.0138	1413	3	2.7	0.9832	163.5 ± 11.4	13.1 ± 0.9
Range front fan	STM5	B	38.7354	106.0138	1411	3	2.8	0.9832	101.9 ± 13.3	8.2 ± 1.1
Range front fan	STM6	B	38.7354	106.0138	1419	3	2.7	0.9832	138.7 ± 6.5	11.1 ± 0.5
Range front fan	STM7	B	38.7349	106.0149	1400	3	2.7	0.9795	219.0 ± 6.7	17.8 ± 0.6
Range front fan	STM8	B	38.7344	106.0150	1399	3	2.7	0.9795	469.0 ± 16.4	38.3 ± 1.4
T5	STM10	A	38.7839	106.1343	1193	2	2.7	0.9996	2288.0 ± 38.3	221.5 ± 3.9
T5	STM11A	C	38.7828	106.1398	1162	4	2.7	0.9996	1560.6 ± 32.5	154.4 ± 3.3
T5	STM11B	C	38.7828	106.1398	1162	4	2.7	0.9996	2161.5 ± 29.8	217.0 ± 3.2
T5	STM11C	C	38.7828	106.1398	1162	4	2.7	0.9996	2094.9 ± 23.4	209.6 ± 2.5
T5	STM11D	C	38.7828	106.1398	1162	4	2.7	0.9996	1084.5 ± 17.0	105.6 ± 1.7
T5	STM11E	C	38.7828	106.1398	1162	4	2.7	0.9996	1820.7 ± 43.3	181.3 ± 4.5
T5	STM11F	C	38.7828	106.1398	1162	4	2.7	0.9996	2215.7 ± 23.4	223.4 ± 2.5
T5	STM11G	C	38.7828	106.1398	1162	4	2.7	0.9996	2134.5 ± 36.8	213.9 ± 3.9
T5	STM11H	C	38.7828	106.1398	1162	4	2.7	0.9996	2054.8 ± 46.8	205.4 ± 4.9
T5 (inheritance)	STM12	A	38.7766	106.1285	1194	2	2.7	0.9996	299.0 ± 7.5	27.5 ± 0.7
T5 (inheritance)	STM13A	C	38.7766	106.1285	1194	4	2.7	0.9996	679.6 ± 12.2	64.3 ± 1.2
T5 (inheritance)	STM13B	C	38.7766	106.1285	1194	4	2.7	0.9996	85.4 ± 3.8	8.0 ± 0.4
T2	STM14	A	38.7047	106.0248	1254	2	2.7	0.9993	209.9 ± 5.5	18.5 ± 0.5
T2	STM14A	C	38.7047	106.0248	1254	4	2.7	0.9993	96.9 ± 3.6	8.7 ± 0.3
T2	STM14B	C	38.7047	106.0248	1254	4	2.7	0.9993	859.5 ± 16.2	78.0 ± 1.5
T2	STM14C	C	38.7047	106.0248	1254	4	2.7	0.9993	110.4 ± 7.7	9.8 ± 0.7
T3	STM15	A	38.7063	106.0270	1251	2	2.7	0.9993	475.7 ± 11.5	42.3 ± 1.0
T2 and T3 (inheritance)	STM16	A	38.7080	106.0330	1264	2	2.7	0.9993	165.0 ± 8.0	14.4 ± 0.7
T2 and T3 (inheritance)	STM16A	C	38.7080	106.0330	1264	5	2.7	0.9993	108.3 ± 3.3	9.7 ± 0.3
T2 and T3 (inheritance)	STM16B	C	38.7080	106.0330	1264	5	2.7	0.9993	226.1 ± 5.4	20.3 ± 0.5
T2 and T3 (inheritance)	STM16C	C	38.7080	106.0330	1264	5	2.7	0.9993	107.4 ± 3.7	9.6 ± 0.3
T2 and T3 (inheritance)	STM16D	C	38.7080	106.0330	1264	5	2.7	0.9993	373.8 ± 8.3	33.6 ± 0.8

[a] A = aggregate of pebbles; B = boulder top; C = clast.

[b] Background-corrected values. Errors are analytical AMS uncertainties for samples and blanks propagated in quadrature. The NIST_ 27900 standard, with a ratio of 2.79×10^{-11}, was used for all samples.

[c] Exposure ages were calculated with the CRONUS-Earth online calculator (version 2.2), using a constant production rate model and a sea level high-latitude reference production rate of 4.49 ± 0.39 atoms g^{-1} yr^{-1} [*Lal*, 1991; *Stone*, 2000; *Balco et al.*, 2008].

overestimate the size of the inherited component, the inheritance is nonetheless much less than the ages from the T5 surface itself. A zero inheritance model gives a T5 age of 221.5 ± 3.9 ka, while the largest measured inheritance (sample 13A) gives a T5 age of 157.2 ± 4.1 ka. These ages correspond to vertical throw rates of 0.09 ± 0.01 mm/a and 0.12 ± 0.01 mm/a, respectively (see Table 2). The large uncertainty in the inheritance therefore has little effect on the calculated throw rate.

4.3. Central Suyukou Scarps

Our second ^{10}Be sampling site was at a location where a major river from the Helanshan crosses the Suyukou scarps and the staircase pattern of aggradational footwall terraces proposed by *Deng and Liao* [1996] can be seen to the southwest of the current channel (see Figure 8). However, our results from this site (see Table 3) suggest that there is significant variation in the magnitude of the inherited component and that the ages

obtained are not sufficiently reliable to determine the precise timing of the earthquakes represented by T2 and T3. Further discussion of the results from this site can therefore be found in the supporting information.

4.4. Helanshan Range Front

4.4.1. Overview and Offset Measurement

Our third throw rate site was at the Helanshan range front, at the location indicated in Figure 8. Here a boulder fan straddles the range front fault and a terrace is preserved either side of the channel on the footwall side (see Figure 10). This terrace predates T1 to T4. Topographic profiles extracted from the Pleiades DEM indicate that the terrace records an offset on the range front fault of 24.0 ± 4.0 m (see Figure 10e and the supporting information for methodology).

4.4.2. Age Constraints and Throw Rate

An amalgamated sample of 83 quartz pebbles (sample 9, from 38.736°N, 106.012°E) and a single boulder top (sample 1, from 38.736°N, 106.011°E) were collected from the terrace surface southwest of the channel (see Figure 10b for locations). We were not able to collect more boulder top samples because there were very few large boulders with well-preserved desert varnish on top of the terrace. The samples yielded ^{10}Be ages of 120.6 ± 1.9 ka and 111.5 ± 2.0 ka, respectively. Despite the small number of samples, the relatively close agreement between the two gives us confidence that the aggregate age is reliable.

We use the aggregate age of 120.6 ± 1.9 ka to calculate a vertical throw rate of 0.20 ± 0.03 mm/a (see Table 2), which is a minimum rate because it does not account for inherited ^{10}Be. If we allow for an inheritance of 64.3 ± 1.2 ka, as measured for sample 13A in a different catchment (although this is almost certainly an overestimate of the inheritance in this system), we obtain a vertical throw rate of 0.43 ± 0.07 mm/a (see Table 2). In other words, even though the uncertainty on the inheritance is large, the maximum throw rate is still small (less than 0.5 mm/a).

In addition, six boulder tops (samples 3 to 8) were collected from the boulder fan that straddles the range front fault (see Figure 10b and Table 3 for locations). Since no scarps are preserved in the boulder fan itself, it must postdate the most recent surface-rupturing event at this location. The boulder tops range in age from 8.2 ± 1.1 ka to 38.3 ± 1.4 ka (see Figure 10f). A plot of ^{10}Be exposure age against distance down slope from the fault trace shows that more distal samples have older exposure ages (see Figure 10g). This suggests that the boulder fan has been generated in more than one event, with the most recent episode of deposition being restricted to near the apex of the fan. Samples 4, 5, and 6, all from near the apex of the fan, have ages of 13.1 ± 0.9, 8.2 ± 1.1, and 11.1 ± 0.5 ka, respectively, and we propose that these three ages represent the probable abandonment age of the boulder fan.

4.5. Northern End of the East Helanshan Fault

4.5.1. Overview and Offset Measurement

At the northern end of the East Helanshan Fault we found evidence for right-lateral motion (see Figure 2 for location). Here three boulder ridges on top of an alluvial fan surface and an incised gully are right laterally offset (see Figure 11). The scarp is fresh, with a free face, and this site is at the northernmost end of the rupture trace from the 1739 Yinchuan earthquake [*Middleton et al.*, 2016]. The incised channel is offset by 4 m (see Figures 11b and 11c), probably representing displacement in the 1739 event. The boulder ridges form indistinct linear markers, but they are not completely aligned by a restoration of 4 m; our best visual restoration is at 16 m, though with visually estimated uncertainties of at least ±5 m (see Figure 11d).

4.5.2. Age Constraints and Slip Rate

We were not able to date the boulder ridge itself because the boulders were poorly preserved and highly weathered. Instead, IRSL samples 4 and 5 were taken from an exposure in the wall of an incised river channel that cuts across the displaced fan (39.236°N, 106.658°E) at depths of 54 cm and 127 cm, respectively. IRSL sample 4 was from a 10 cm thick lens of medium brown silt, covered by a 50 cm thick layer of large, poorly sorted cobbles (see Figure 11e); IRSL sample 5 was from a stratigraphically lower, 20 cm thick layer of orange sand surrounded by coarse gravels and cobbles (see Figure 11f). Sample 4 provided an age of 1.27 ± 0.14 ka, and sample 5 returned an age of 3.21 ± 0.21 ka (see Table 1). These results are stratigraphically consistent.

The 1.27 ka age implies a horizontal slip rate of 12.6 ± 4.2 mm/a, which appears unrealistically large, while the 3.21 ka age implies a horizontal slip rate of 5.0 ± 1.6 mm/a (see Table 2). However, we note that both samples were taken from the fill of a channel between the boulder ridges, which probably postdates abandonment

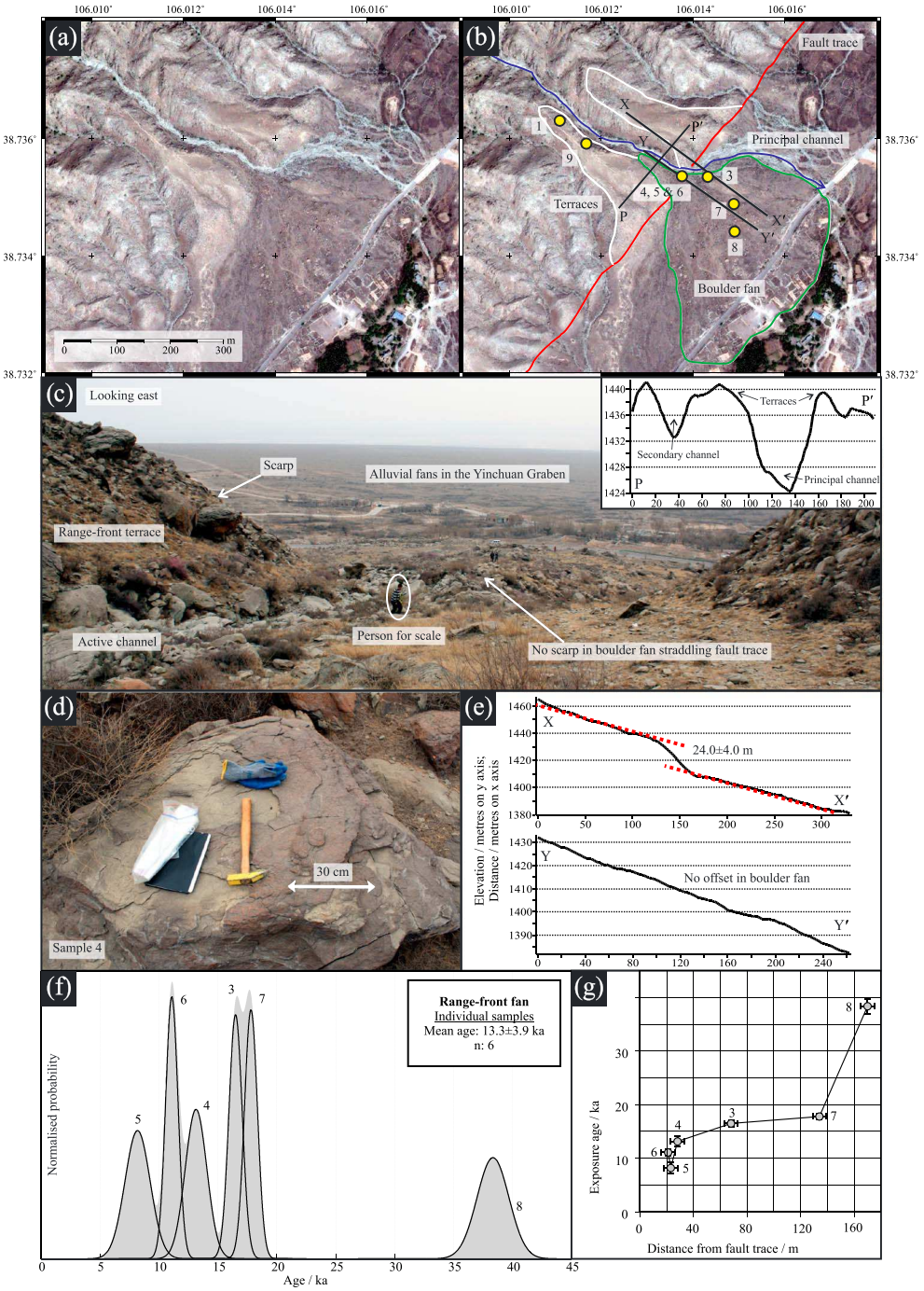

Figure 10. (a) Pleiades imagery of the range front fault on the eastern flank of the Helanshan. (b) Annotated version of Figure 10a showing fault trace (in red), two uplifted footwall terraces (in white), and an alluvial fan that has been deposited on top of the fault (in green). Yellow circles mark locations where boulder tops were collected for ^{10}Be exposure dating. (c) Annotated field photograph (taken at 38.735°N, 106.014°E) looking from the footwall, across the range front fault trace, toward the boulder fan in the hanging wall. Inset shows topographic profile along the line P-P′ in Figure 10b, illustrating the terraces either side of the main channel. (d) Field photograph (taken at 38.735°N, 106.014°E) showing desert varnish on the top of the boulder where sample 4 was collected. (e) Topographic profiles from the Pleiades DEM along the lines marked X-X′ and Y-Y′ in Figure 10b. (f) ^{10}Be age results for the range front fan. The black curves are normally distributed probability density functions (PDFs) for individual samples, defined by their age and 1σ analytical error. The grey curve is a normal kernel density estimate (or camel plot), obtained by summing the individual PDFs. (g) Plot of ^{10}Be exposure age for boulder top samples from the range front fan against their distance from the fault trace. Error bars show 1σ analytical error on age measurements and an assumed error of ±5 m on the distance measurements.

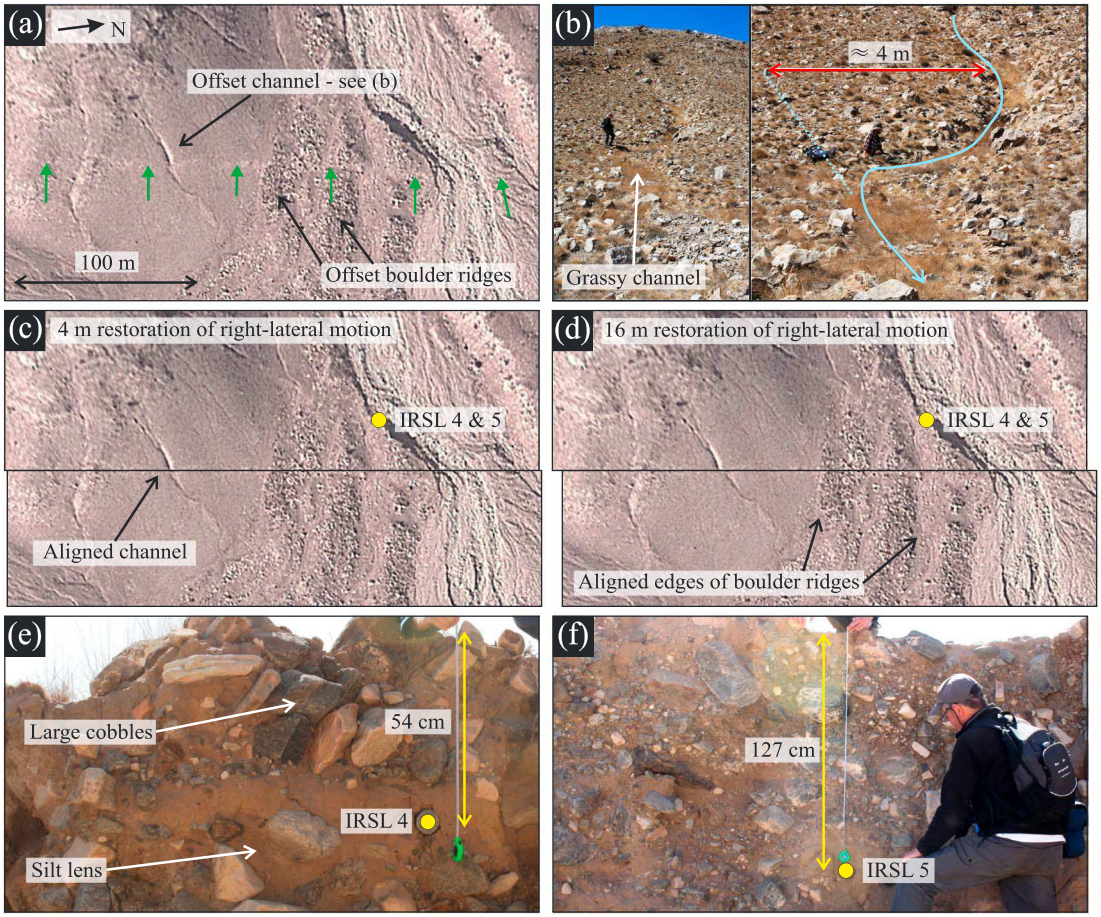

Figure 11. (a) Google Earth imagery from November 2011 (source: http://earth.google.com) of the northern end of the East Helanshan Fault (see Figure 2 for location). Fault scarp marked by green arrows and small offset visible in edges of boulder ridges. (b) Field photographs (taken at 39.235°N, 106.658°E, at the location marked in Figure 11a). People for scale. The grassy channel records a right-lateral offset of approximately 4 m. (c) Same as Figure 11a with a 4 m restoration of the right-lateral motion, which aligns the small channel shown in Figure 11b. Yellow circle indicates the location of IRSL samples 4 and 5. (d) Same as Figure 11a with a 16 m restoration of the right-lateral motion, which aligns the edges of the boulder ridges as shown. Yellow circle indicates the location of IRSL samples 4 and 5. (e) Field photograph (taken at 39.236°N, 106.658°E) showing the sedimentary context of IRSL sample 4. (f) Field photograph (from the same location) showing the sedimentary context of IRSL sample 5.

of the fan itself. It is hence likely that both IRSL ages underestimate the deposition age of the underlying displaced boulder ridge. If this is the case, then our rate of 5.0 ± 1.6 mm/a only provides a maximum bound on the slip rate.

5. Discussion

5.1. Rates of Faulting Along the Western Ordos Plateau

Our key result from the Luoshan Fault is that the slip rate is comparatively large (i.e., >4 mm/a), which shows that this fault is one of the principal active structures in the western Ordos region. The agreement between our slip rate results from IRSL samples 2 and 3 (to within their 1σ analytical errors), and our reassessment of the Shiyaodong site indicates that the mean right-lateral Holocene slip rate on the Luoshan Fault is 4.3 ± 0.4 mm/a (where the error now refers to the weighted standard deviation of the three slip rate estimates; see Table 2). Furthermore, at all three sites the fans were dated to approximately 10 ka ago (and the measured horizontal offsets are similar). This common age suggests that the deposition of these fans is principally controlled by climate, possibly the ending of the Younger Dryas period around 11.7 ka ago. This sort of climatic control on fan deposition has previously been suggested in a number of other locations, such as western Mongolia, southern California, and the margins of the Tibetan Plateau [*Nissen et al.*, 2009; *Ganev et al.*, 2012; *Hetzel*, 2013].

On the East Helanshan Fault our major result is that the throw rate, and hence the extension rate, is comparatively small (i.e., <1 mm/a). Since the Suyukou scarps run parallel to the Helanshan range front, we add our

maximum throw rate estimate from T5 on the Suyukou scarps (of 0.12 ± 0.01 mm/a) to our maximum throw rate estimate from the range front (of 0.43 ± 0.07 mm/a) to obtain a maximum late Quaternary throw rate for the fault as a whole of 0.6 ± 0.1 mm/a (see Table 2). This is consistent with the Quaternary average of 0.5 to 0.8 mm/a from *Zhang et al.* [1990]. Using the fault dip found in the literature of 39° [*Fang et al.*, 2009], we find a maximum extension rate across the East Helanshan Fault of 0.7 ± 0.1 mm/a (see Table 2). If we also include the throw rates and fault dips of the other faults within the graben (Yellow River Fault: 0.25 mm/a and 72° [*Liao et al.*, 2000; *Fang et al.*, 2009]; Yinchuan-Pingluo Fault: 0.14 mm/a and 71° [*Lei et al.*, 2008, 2015]; and Luhuatai Fault: 0.18 mm/a and 60° [*Fang et al.*, 2009; *Lei et al.*, 2011]), we obtain a maximum extension rate across the whole graben of 0.9 ± 0.1 mm/a.

Campaign GPS measurements [*Zhao et al.*, 2015] also indicate that right-lateral shearing is the major motion occurring in the western Ordos region (see Figure 12). Figure 12a shows the data from *Zhao et al.* [2015] with a best fitting rigid-body rotation (about an Euler pole at 46°N, 72°W, estimated from the vectors within this region) subtracted from all of the vectors. This ensures that rotations associated with this rigid-body-like motion do not distort our slip rate estimates. We model the fault-parallel interseismic motion across the Luoshan Fault as a buried screw dislocation in an elastic half-space using the formulation from *Savage and Burford* [1973], where the velocity u at a perpendicular distance x from the fault is given by $u = \frac{s}{\pi}\tan^{-1}\left(\frac{x}{d}\right)$, where s is the slip rate and d is the locking depth. The density of data is not sufficient to provide an independent constraint on the locking depth, so we assume locking depths in the range of 15 to 30 km in order to calculate the distribution of possible slip rate estimates [*Wright et al.*, 2013]. Earthquake epicenters in the region are known to extend to a maximum depth of ≈ 22 km [*Molnar et al.*, 1984; *Li et al.*, 2015]. In Figure 12b, the range of possible arctangent functions fitted to the data indicates a right-lateral slip rate on the Luoshan and northern Yunwushan Faults of 4.5 ± 0.7 mm/a. Our geological slip rate of 4.3 ± 0.4 mm/a agrees well with this geodetic rate. We also note that one GPS point lies noticeably to the west of our best fitting curves. This may indicate that the center of the shear zone at depth is displaced to the west of the surface trace of the Luoshan Fault, but there is not enough data to test this. Figure 12c shows that although the errors on the data are large, there is no resolvable fault-perpendicular motion along profile X-X′; significant crustal shortening only occurs farther to the south of our profile.

The data in Figure 12d, for profile Y-Y′ across the Yinchuan Graben, are more scattered than in Figure 12b. If we assume that all of the right-lateral motion is localized onto a single structure, we obtain a right-lateral slip rate of 3.3 ± 0.5 mm/a (allowing for the same 15 to 30 km range of locking depths). However, the scatter in the data suggests that it is more likely that right-lateral motion is distributed across a number of the buried faults within the Yinchuan Graben. In Figure 12e, the scatter in the data is again very large—and extension is barely resolvable—but we obtain a best fitting extension rate of 1.3 ± 1.6 mm/a across the Yinchuan Graben. This is consistent with our late Quaternary extension rate of 0.9 ± 0.1 mm/a and also supports our suggestion that right-lateral motion is dominant over the extension in the Yinchuan Graben. For comparison, *Wang et al.* [2011] fitted a block model to the GPS data of *Zhang and Gan* [2008] and obtained predicted fault slip rates in the Yinchuan Graben of 2.6 ± 0.5 mm/a (right lateral) and 1.0 ± 0.5 mm/a (extensional). These rates are slightly smaller than our results because *Wang et al.* [2011] used a smaller locking depth of 10 km, but they nonetheless agree to within their quoted errors.

5.2. A Geometric Model for the Western Ordos Plateau

We propose a geometric model in which the faults of the western Ordos Plateau accommodate principally north-south right-lateral shearing. This occurs on the Luoshan Fault in the south and is likely to be distributed across a number of different faults in the north (see Figure 13). The Niushoushan Fault is known to accommodate ≈0.4 mm/a of right-lateral motion at the southern end of the Yinchuan Graben [*Lei et al.*, 2016], and our observations of offset boulder ridges at the northern end of the East Helanshan Fault provide evidence for right-lateral motion at the northern end of the graben (see section 4.5). It is also possible that right-lateral motion is taken up by the Alxa Desert Fault and some of the buried faults within the Yinchuan Graben. A Kostrov summation for the two largest earthquakes in northern Ningxia in the last 700 years indicates that north-south right-lateral motion is one of the most significant strains [*Wesnousky et al.*, 1984]. Furthermore, one of the few focal mechanisms from the instrumental record (for a M_w 5.2 event in 1988—see Figure 2) is also consistent with north-south right-lateral motion.

In addition, we suggest that the (oblique reverse) Niushoushan Fault accommodates transpression as the strike-slip faulting steps to the left and that the normal faulting in the Yinchuan Graben accommodates

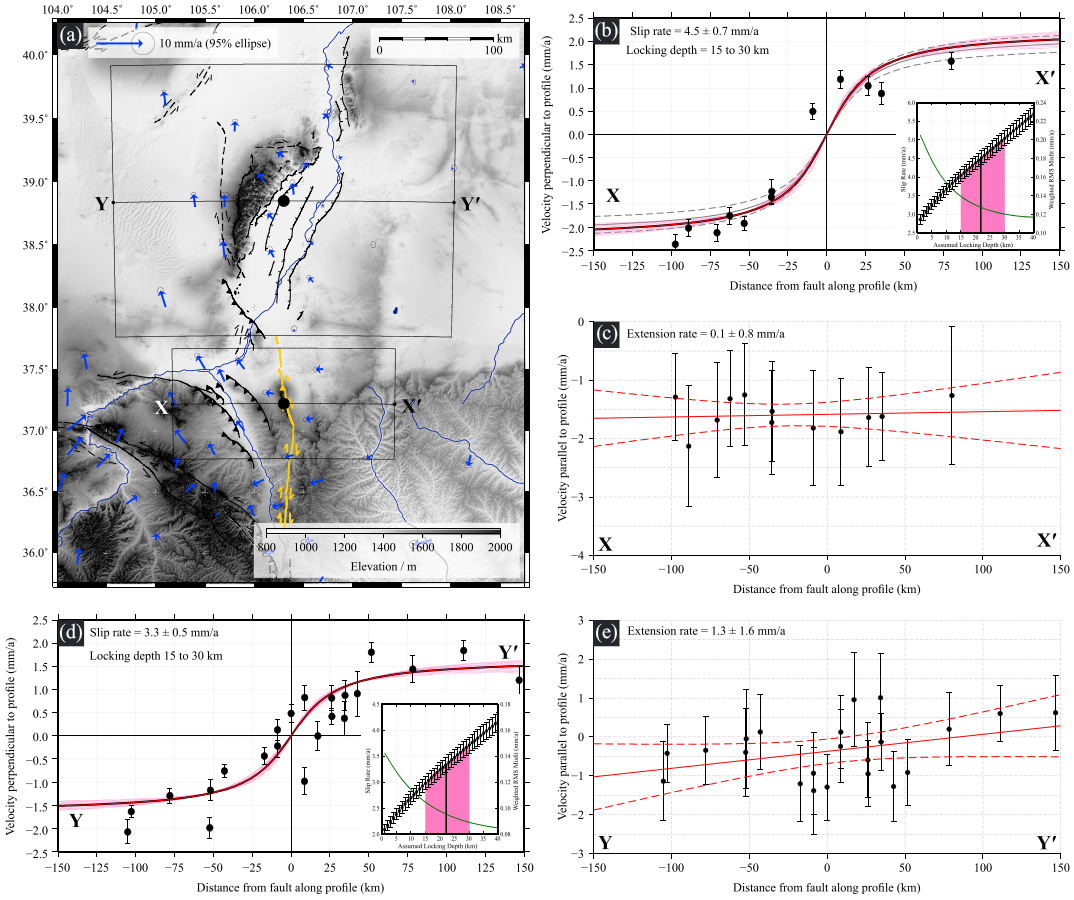

Figure 12. (a) SRTM topography (30 m resolution) of the western Ordos region, Ningxia Province, northern China [*Farr et al.*, 2007]. The Luoshan Fault and Yunwushan Fault are marked in orange. Blue vectors show campaign GPS measurements made over a period of 4 years (occupations in 2009, 2011, and 2013) [*Zhao et al.*, 2015] with a best fitting rigid-body rotation (about an Euler pole at 46°N, 72°W, estimated from the vectors within this region) subtracted from all of the vectors. (b) Swath profile X-X′ through the GPS data showing the component of velocity perpendicular to the profile azimuth of 90°. The red line shows the best fitting arctangent function ($u = \tan^{-1}\left(\frac{x}{d}\right)$, where u is the velocity, x is the distance from the fault, and d is the locking depth). The dashed grey lines indicate the geologically determined slip rate on the Luoshan Fault of 4.3 ± 0.4 mm/a, assuming a locking depth of 22 km. The pink lines represent the range of best fitting solutions for assumed locking depths of between 15 and 30 km. The inset figure shows the trade-off between slip rate and locking depth. For this range of locking depths, we estimate a right-lateral slip rate of 4.5 ± 0.7 mm/a. (c) Swath profile X-X′ showing the component of velocity parallel to the profile. The red lines show the best fit least squares regression to the data and the 95% confidence envelopes on this best fit line. No shortening or extension is resolvable within error along this profile. (d) Swath profile Y-Y′ through the GPS data in the Yinchuan Graben showing the component of velocity perpendicular to the profile. Annotations as in Figure 12b. We estimate a right-lateral slip rate of 3.3 ± 0.5 mm/a. (e) Swath profile Y-Y′ showing the component of velocity parallel to the profile. Annotations as in Figure 12c. We estimate an average extension rate across the whole profile of 1.3 ± 1.6 mm/a.

transtension as the strike-slip faulting steps to the right. The estimated slip vector for the most recent earthquake on the East Helanshan Fault appears to show pure normal motion [*Middleton et al.*, 2016]. We therefore speculate that the transtension in the Yinchuan Graben is partitioned between normal motion on the East Helanshan Fault and right-lateral strike-slip motion on one or more of the buried faults within the graben (i.e., the Luhuatai, Yinchuan-Pingluo, or Yellow River Fault).

5.3. Implications for the Kinematics of the Ordos Block

In section 1 we observed that the Ordos Plateau is situated within a large-scale zone of WNW-ESE left-lateral shearing and several kinematic models have proposed that the plateau is rotating anticlockwise within this zone of shearing [*Xu and Ma*, 1992; *Xu et al.*, 1993; *Avouac and Tapponnier*, 1993; *Xu et al.*, 1994; *Zhang et al.*, 1995; *Peltzer and Saucier*, 1996; *Zhang et al.*, 1998]. We have shown that the anticlockwise rotation of the Ordos

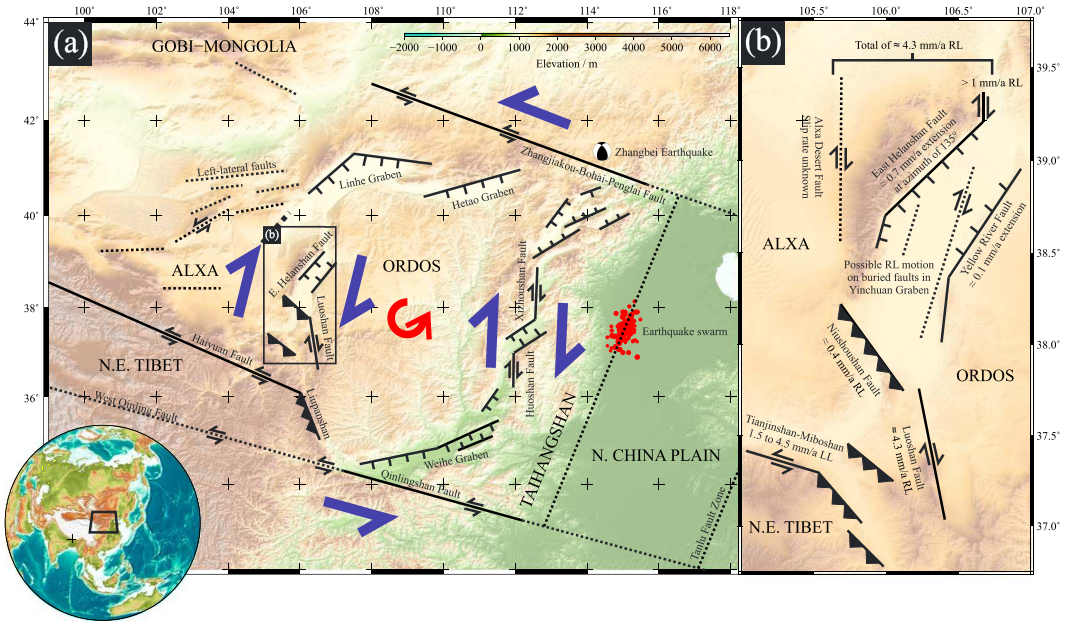

Figure 13. (a) SRTM topography (90 m resolution) of the Ordos Plateau in northeastern China [*Farr et al.*, 2007]. Inset globe shows the location of Figure 13a within Asia. Black lines indicate major faults or fault zones and their sense of movement. Dotted lines show possible additional blocks—the Taihangshan and North China Plain blocks—to the east of the Ordos Plateau. General kinematic scheme after *Xu and Ma* [1992], *Xu et al.* [1993], and *Xu et al.* [1994]. (b) Geometric model for the tectonics of the western Ordos region showing the principal faults and their slip rates, from *Zhang et al.* [1990], *Min et al.* [2003], *Deng et al.* [2007], and this study.

block can be confirmed by considering the fault kinematics at the boundaries of the block. For an equidimensional crustal block that is rotating within a large-scale shear zone, the second-order strike-slip motion on either side of the block is expected to be of a similar magnitude and opposite sense to the overall shear gradient across the block. In the case of the Ordos Plateau, the GPS data in Figure 1c indicate an overall left-lateral shear gradient across the block of ≈5 mm/a. Meanwhile, we have shown in this study that the dominant motion on the western side of the block is right lateral, at a rate of ≈4 mm/a. Right-lateral shearing also occurs on the eastern side of the block by normal slip on the en echelon Shanxi Grabens and right-lateral slip on the Xizhoushan Fault (at 5.7 mm/a) and the Huoshan Fault (at 5.0 mm/a) [*Xu et al.*, 1986; *Xu and Deng*, 1990; *Xu et al.*, 1993]. In other words, the Ordos Plateau behaves as expected, with the second-order strike-slip motion on either side of the block occurring at a similar rate but in the opposite sense to the motion of the overall shear zone (see Figure 13).

The apparent predominance of normal faulting around the margins of the Ordos Plateau disguises the fact that it is the strike-slip motions that are most important. The normal faulting is present either as part of a partitioned transtensional system (as may be the case for the East Helanshan Fault) or because it is arranged en echelon to accommodate an overall shear (as is the case in the Shanxi Grabens). Similar tectonic arrangements of rotating crustal blocks are also seen elsewhere—for example, in northern Israel [*Ron et al.*, 1984], eastern Iran [*McKenzie and Jackson*, 1983; *Walker and Jackson*, 2004], the Walker Lane of western North America [*Wesnousky*, 2005; *Wesnousky et al.*, 2012], and the southeastern Tibetan Plateau [*Copley*, 2008].

6. Conclusions

In the absence of reliable paleomagnetic constraints, we have used the fault kinematics in the western Ordos region to examine the hypothesis that the Ordos Plateau acts as a rigid crustal block within a large-scale left-lateral shear zone, rotating anticlockwise about a vertical axis. Our key result is that the rate of strike-slip motion on the Luoshan Fault (4.3 ± 0.4 mm/a) is substantially larger than the throw rate on the normal East Helanshan Fault ($<0.6 \pm 0.1$ mm/a). We therefore conclude that north-south right-lateral shearing is the principal tectonic motion in the western Ordos region, which is compatible with anticlockwise rotation of the whole Ordos block.

Acknowledgments
This research has been supported by the Natural Environment Research Council (NERC) through a studentship awarded to T.A.M., the Centre for Observation and Modelling of Earthquakes, Volcanoes and Tectonics (COMET, GA/13/M/031), the Looking inside the Continents from Space (LiCS) large grant (NE/K011006/1), the NERC/ESRC Earthquakes without Frontiers (EwF) consortium (EwF_NE/J02001X/1_1), the National Natural Science Foundation of China (41472201), and the State Key Laboratory of Earthquake Dynamics (LED2014A03). We are grateful to Peizhen Zhang and colleagues at the China Earthquake Administration (CEA) for assistance with fieldwork; Victoria Forbes, Maria Miguens-Rodriguez, Kathy Keefe, and Owen Green for their help preparing the ^{10}Be samples for dating; Rob Ashurst for his assistance with the IRSL dating; and Al Sloan, Austin Elliott, and David Mackenzie for their helpful discussions. We also wish to thank Marie-Luce Chevalier, an anonymous reviewer, and the Associate Editor for their helpful comments on the manuscript. The Pleiades topography can be downloaded from OpenTopography (http://www.opentopography.org/). Most of the figures in this paper were made using GMT [*Wessel et al.*, 2013].

References

Avouac, J.-P., and P. Tapponnier (1993), Kinematic model of active deformation in central Asia, *Geophys. Res. Lett.*, *20*(10), 895–898, doi:10.1029/93GL00128.

Balco, G., J. O. Stone, N. A. Lifton, and T. J. Dunai (2008), A complete and easily accessible means of calculating surface exposure ages or erosion rates from ^{10}Be and ^{26}Al measurements, *Quat. Geochronol.*, *3*(3), 174–195, doi:10.1016/j.quageo.2007.12.001.

Benedetti, L. C., and J. van der Woerd (2014), Cosmogenic nuclide dating of earthquakes, faults, and toppled blocks, *Elements*, *10*, 357–362, doi:10.2113/gselements.10.5.357.

Burchfiel, B., P. Zhang, Y. Wang, W. Zhang, F. Song, Q. Deng, P. Molnar, and L. Royden (1991), Geology of the Haiyuan Fault Zone, Ningxia-Hui Autonomous Region, China, and its relation to the evolution of the Northeastern Margin of the Tibetan Plateau, *Tectonics*, *10*(6), 1091–1110, doi:10.1029/90TC02685.

Buylaert, J. P., A. Murray, K. J. Thomsen, and M. Jain (2009), Testing the potential of an elevated temperature IRSL signal from K-feldspar, *Radiat. Meas.*, *44*(5–6), 560–565, doi:10.1016/j.radmeas.2009.02.007.

Copley, A. (2008), Kinematics and dynamics of the southeastern margin of the Tibetan Plateau, *Geophys. J. Int.*, *174*, 1081–1100, doi:10.1111/j.1365-246X.2008.03853.x.

Cowgill, E. (2007), Impact of riser reconstructions on estimation of secular variation in rates of strike-slip faulting: Revisiting the Cherchen River site along the Altyn Tagh Fault, NW China, *Earth Planet. Sci. Lett.*, *254*, 239–255, doi:10.1016/j.epsl.2006.09.015.

Darby, B., B. Ritts, Y. Yue, and Q. Meng (2005), Did the Altyn Tagh fault extend beyond the Tibetan Plateau?, *Earth Planet. Sci. Lett.*, *240*(2), 425–435, doi:10.1016/j.epsl.2005.09.011.

Darby, B. J., and B. D. Ritts (2002), Mesozoic contractional deformation in the middle of the Asian tectonic collage: The intraplate Western Ordos fold-thrust belt, China, *Earth Planet. Sci. Lett.*, *205*(1–2), 13–24, doi:10.1016/S0012-821X(02)01026-9.

DeMets, C., R. G. Gordon, D. F. Argus, and S. Stein (1990), Current plate motions, *Geophys. J. Int.*, *101*(2), 425–478, doi:10.1111/j.1365-246X.1990.tb06579.x.

DeMets, C., R. G. Gordon, D. F. Argus, and S. Stein (1994), Effect of recent revisions to the geomagnetic reversal time scale on estimates of current plate motions, *Geophys. Res. Lett.*, *21*(20), 2191–2194, doi:10.1029/94GL02118.

Deng, Q., and Y. Liao (1996), Paleoseismology along the range-front fault of Helan Mountains, north central China, *J. Geophys. Res.*, *101*, 5873–5893.

Deng, Q., F. Sung, S. Zhu, M. Li, T. Wang, W. Zhang, B. C. Burchfiel, P. Molnar, and P. Zhang (1984), Active faulting and tectonics of the Ningxia-Hui Autonomous Region, China, *J. Geophys. Res.*, *89*, 4427–4445.

Deng, Q., Y. Ran, X. Yang, W. Min, and Q. Chu (2007), *Map of Active Tectonics in China* [in Chinese], Seismological Press, Beijing.

Ekström, G., M. Nettles, and A. Dziewonski (2012), The global CMT project 2004–2010: Centroid-moment tensors for 13,017 earthquakes, *Phys. Earth Planet. Inter.*, *200–201*, 1–9, doi:10.1016/j.pepi.2012.04.002.

Elliott, A. J., M. E. Oskin, J. Liu, and Y. Shao (2015), Rupture termination at restraining bends: The last great earthquake on the Altyn Tagh Fault, *Geophys. Res. Lett.*, *42*(7), 2164–2170, doi:10.1002/2015GL063107.

England, P., and P. Molnar (1997), The field of crustal velocity in Asia calculated from Quaternary rates of slip on faults, *Geophys. J. Int.*, *130*, 551–582.

Fan, J., and J. Ma (2003), Movement of Ordos block and alternation of activity along its boundaries, *Sci. China, Ser. D Earth Sci.*, *46*, 168–180, doi:10.1360/03dz0013.

Fang, S., C. Zhao, C. Chai, B. Liu, S. Feng, M. Liu, Q. Lei, and H. Liu (2009), Seismological evidences of the crustal structures and tectonics in the Yinchuan Downfaulted Basin, *Chin. J. Geophys.*, *52*(5), 1101–1110, doi:10.1002/cjg2.1435.

Farr, T. G., et al. (2007), The Shuttle Radar Topography Mission, *Rev. Geophys.*, *45*(2), 1–33, doi:10.1029/2005RG000183.

Frankel, K. L., and J. F. Dolan (2007), Characterizing arid region alluvial fan surface roughness with airborne laser swath mapping digital topographic data, *J. Geophys. Res.*, *112*(2), 1–14, doi:10.1029/2006JF000644.

Gan, W., P. Zhang, Z.-K. Shen, Z. Niu, M. Wang, Y. Wan, D. Zhou, and J. Cheng (2007), Present-day crustal motion within the Tibetan Plateau inferred from GPS measurements, *J. Geophys. Res.*, *112*(B8), 1–14, doi:10.1029/2005JB004120.

Ganev, P. N., J. F. Dolan, S. F. McGill, and K. L. Frankel (2012), Constancy of geologic slip rate along the central Garlock fault: Implications for strain accumulation and release in southern California, *Geophys. J. Int.*, *190*(2), 745–760, doi:10.1111/j.1365-246X.2012.05494.x.

Gosse, J. C., and F. M. Phillips (2001), Terrestrial in situ cosmogenic nuclides: Theory and application, *Quat. Sci. Rev.*, *20*(14), 1475–1560, doi:10.1016/S0277-3791(00)00171-2.

Granger, D. E., and M. Schaller (2014), Cosmogenic nuclides and erosion at the watershed scale, *Elements*, *10*, 369–374, doi:10.2113/gselements.10.5.369.

Hetzel, R. (2013), Active faulting, mountain growth, and erosion at the margins of the Tibetan Plateau constrained by in situ-produced cosmogenic nuclides, *Tectonophysics*, *582*, 1–24, doi:10.1016/j.tecto.2012.10.027.

Huntley, D. J., D. I. Godfrey-Smith, and M. L. W. Thewalt (1985), Optical dating of sediments, *Nature*, *313*, 105–107.

Hütt, G., I. Jaek, and J. Tchonka (1988), Optical dating: K-feldspars optical response stimulation spectra, *Quat. Sci. Rev.*, *7*, 381–385, doi:10.1016/0277-3791(88)90033-9.

Jackson, J., and D. McKenzie (1988), The relationship between plate motions and seismic moment tensors, and the rates of active deformation in the Mediterranean and Middle East, *Geophys. J. Int.*, *93*(1), 45–73, doi:10.1111/j.1365-246X.1988.tb01387.x.

Lal, D. (1991), Cosmic ray labeling of erosion surfaces: In situ nuclide production rates and erosion models, *Earth Planet. Sci. Lett.*, *104*, 424–439.

Lamothe, M., S. Balescu, and M. Auclair (1994), Natural IRSL intensities and apparent luminescence ages of single feldspar grains extracted from partially bleached sediments, *Radiat. Meas.*, *23*(2–3), 555–561, doi:10.1016/1350-4487(94)90099-X.

Lasserre, C., Y. Gaudemer, P. Tapponnier, A.-S. Mériaux, J. Van der Woerd, Y. Daoyang, F. Ryerson, R. Finkel, and M. Caffee (2002), Fast late Pleistocene slip rate on the Leng Long Ling segment of the Haiyuan Fault, Qinghai, China, *J. Geophys. Res.*, *107*, 2276, doi:10.1029/2000JB000060.

Lawson, M. J., B. J. Roder, D. M. Stang, and E. J. Rhodes (2012), OSL and IRSL characteristics of quartz and feldspar from southern California, USA, *Radiat. Meas.*, *47*(9), 830–836, doi:10.1016/j.radmeas.2012.03.025.

Lei, Q., C. Chai, G. Meng, P. Du, Y. Wang, X. Xie, and X. Zhang (2008), Composite drilling section exploration of Yinchuan Buried Fault [in Chinese], *Seismolog. Geol.*, *30*(1), 250–263.

Lei, Q., C. Chai, P. Du, Y. Wang, and G. Meng (2011), Activity characteristics of Luhuatai Buried Fault since Late Quaternary revealed by drilling [in Chinese], *Seismolog. Geol.*, *33*(3), 602–614.

Lei, Q., C. Chai, P. Du, J. Yu, X. Xie, and Y. Wang (2015), Re-discussion of the seismogenic structure of the M8.0 Pingluo earthquake in 1739 [in Chinese], *Seismolog. Geol.*, *37*(2), 413–429.

Lei, Q., P. Zhang, W. Zheng, C. Chai, W. Wang, P. Du, and J. Yu (2016), Dextral strike-slip of Sanguankou-Niushoushan fault zone and extension of arc tectonic belt in the northeastern margin of the Tibet Plateau, *Sci. China Earth Sci.*, *59*(5), 1025–1040, doi:10.1007/s11430-016-5272-1.

Li, B., K. Atakan, M. B. Sørensen, and J. Havskov (2015), Stress pattern of the Shanxi rift system, North China, inferred from the inversion of new focal mechanisms, *Geophys. J. Int.*, *201*(2), 505–527, doi:10.1093/gji/ggv025.

Li, C., P. Zhang, J. Yin, and W. Min (2009), Late Quaternary left-lateral slip rate of the Haiyuan fault, northeastern margin of the Tibetan Plateau, *Tectonics*, *28*, 1–26, doi:10.1029/2008TC002302.

Li, W., Y. Lu, and G. Ding (2001), Paleomagnetic evidence from loess for the relative motion between the Ordos and its adjacent blocks [in Chinese], *Quat. Sci.*, *21*(6), 551–559.

Li, W., Y. Dong, A. Guo, X. Liu, and D. Zhou (2013), Chronology and tectonic significance of Cenozoic faults in the Liupanshan Arcuate Tectonic Belt at the northeastern margin of the Qinghai-Tibet Plateau, *J. Asian Earth Sci.*, *73*, 103–113, doi:10.1016/j.jseaes.2013.04.026.

Liao, Y., and Z. Pan (1982), Dislocation of the great wall in the Hongguozigou, Ningxia autonomous region [in Chinese], *Seismolog. Geol.*, *4*(2), 77–80.

Liao, Y., C. Chai, W. Zhang, and W. Xu (2000), The active features and slip rate of Lingwu faults in late Quaternary, *Earthquake Res. China*, *16*(2), 158–165.

Liu, M., X. Cui, and F. Liu (2004), Cenozoic rifting and volcanism in Eastern China: A mantle dynamic link to the Indo Asian collision?, *Tectonophysics*, *393*(1–4), 29–42, doi:10.1016/j.tecto.2004.07.029.

Liu, M., S. Stein, and H. Wang (2011), 2000 years of migrating earthquakes in North China: How earthquakes in midcontinents differ from those at plate boundaries, *Lithosphere*, *3*(2), 128–132, doi:10.1130/L129.1.

Liu-Zeng, J., Y. Klinger, X. Xu, C. Lasserre, G. Chen, W. Chen, P. Tapponnier, and B. Zhang (2007), Millennial recurrence of large earthquakes on the Haiyuan fault near Songshan, Gansu Province, China, *Bull. Seismol. Soc. Am.*, *97*(1B), 14–34, doi:10.1785/0120050118.

McKenzie, D., and J. Jackson (1983), The relationship between strain rates, crustal thickening, palaeomagnetism, finite strain and fault movements within a deforming zone, *Earth Planet. Sci. Lett.*, *65*(1), 182–202, doi:10.1016/0012-821X(83)90198-X.

Middleton, T. A., R. T. Walker, B. Parsons, Q. Lei, Y. Zhou, and Z. Ren (2016), A major, intraplate, normal-faulting earthquake: The 1739 Yinchuan event in northern China, *J. Geophys. Res. Solid Earth*, *121*(1), 293–320, doi:10.1002/2015JB012355.

Min, W., Z. Chai, P. Wang, P. Yang, C. Chai, P. Wang, and P. Yang (1992), Preliminary study on the Holocene active fault features at the eastern piedmont of the Luoshan Mountain [in Chinese], *Earthquake Res. China*, *8*(4), 49–54.

Min, W., Z. Chai, P. Wang, and P. Yang (1993), The study on the paleoearthquakes on the eastern Piedmont fault of the Luoshan Mountains in Holocene [in Chinese], *Earthquake Res. China*, *5*(4), 97–102.

Min, W., P. Zhang, and Q. Deng (2000), Primary study on regional paleoearthquake recurrence behavior, *Acta Seismol. Sin.*, *13*(2), 180–188, doi:10.1007/s11589-000-0008-9.

Min, W., P. Zhang, and Q. Deng (2001), The study of Holocene paleoearthquakes on Zhongwei-Tongxin fault zone [in Chinese], *Seismolog. Geol.*, *3*(23), 357–366.

Min, W., D. Jiao, C. Chai, P. Zhang, and F. Mao (2003), Characteristics of the active Luoshan Fault since Late Pleistocene, North Central China, *Ann. Geophys.*, *46*(5), 997–1013.

Molnar, P., and K. E. Dayem (2010), Major intracontinental strike-slip faults and contrasts in lithospheric strength, *Geosphere*, *6*(4), 444–467, doi:10.1130/GES00519.1.

Molnar, P., D. Qidong, and Q. Deng (1984), Faulting associated with large earthquakes and the average rate of deformation in central and eastern Asia, *J. Geophys. Res.*, *89*, 6203–6228, doi:10.1029/JB089iB07p06203.

Murray, A. S., and A. G. Wintle (2000), Luminescence dating of quartz using an improved single-aliquot regenerative-dose protocol, *Radiat. Meas.*, *32*, 57–73.

Neudorf, C. M., R. G. Roberts, and Z. Jacobs (2012), Sources of overdispersion in a K-rich feldspar sample from north-central India: Insights from De, K content and IRSL age distributions for individual grains, *Radiat. Meas.*, *47*(9), 696–702, doi:10.1016/j.radmeas.2012.04.005.

Nie, Z., and W. Lin (1993), Middle segment of Zhongwei-Tongxin fault zone: Seismic deformation band of 1709 earthquake with M 7.5 along Xiangshan-Tianjingshan fault zone [in Chinese], *Earthquake*, *2*(1), 41–44.

Nishiizumi, K., M. Imamura, M. W. Caffee, J. R. Southon, R. C. Finkel, and J. McAninch (2007), Absolute calibration of ^{10}Be AMS standards, *Nucl. Instrum. Methods Phys. Res., Sect. B*, *258*(2), 403–413, doi:10.1016/j.nimb.2007.01.297.

Nissen, E., R. T. Walker, A. Bayasgalan, A. Carter, M. Fattahi, E. Molor, C. Schnabel, A. J. West, and S. Xu (2009), The late Quaternary slip-rate of the Har-Us-Nuur fault (Mongolian Altai) from cosmogenic ^{10}Be and luminescence dating, *Earth Planet. Sci. Lett.*, *286*(3–4), 467–478, doi:10.1016/j.epsl.2009.06.048.

Northrup, C. J., L. H. Royden, and B. C. Burchfiel (1995), Motion of the Pacific Plate relative to Eurasia and its potential relation to Cenozoic extension along the eastern margin of Eurasia, *Geology*, *23*, 719–722, doi:10.1130/0091-7613(1995)023<0719:MOTPPR>2.3.CO;2.

Parsons, B., Y. Zhou, J. Elliott, I. Barisin, and R. Walker (2014), *Assessing the Ability of Pleiades Stereo Imagery to Determine Height Changes in Earthquakes: A Case Study for the El Mayor-Cucapah Epicentral Area*, Abstract EP43E-08 presented at 2014 Fall Meeting, AGU, San Francisco, Calif., 15–19 Dec.

Peltzer, G., and F. Saucier (1996), Present-day kinematics of Asia derived from geologic fault rates, *J. Geophys. Res.*, *101*, 27,943–27,956, doi:10.1029/96JB02698.

Reimann, T., K. J. Thomsen, M. Jain, A. S. Murray, and M. Frechen (2012), Single-grain dating of young sediments using the pIRIR signal from feldspar, *Quat. Geochronol.*, *11*, 28–41, doi:10.1016/j.quageo.2012.04.016.

Ren, Z., Z. Zhang, T. Chen, S. Yan, J. Yin, P. Zhang, W. Zheng, H. Zhang, and C. Li (2015), Clustering of offsets on the Haiyuan fault and their relationship to paleoearthquakes, *Geol. Soc. Am. Bull.*, *128*, 4–18, doi:10.1130/B31155.1.

Rhodes, E. J. (2011), Optically stimulated luminescence dating of sediments over the past 200,000 years, *Annu. Rev. Earth Planet. Sci.*, *39*(1), 461–488, doi:10.1146/annurev-earth-040610-133425.

Rhodes, E. J. (2015), Dating sediments using potassium feldspar single-grain IRSL: Initial methodological considerations, *Quat. Int.*, *362*, 14–22, doi:10.1016/j.quaint.2014.12.012.

Ron, H., R. Freund, Z. Garfunkel, and A. Nur (1984), Block rotation by strike-slip faulting: Structural and paleomagnetic evidence, *J. Geophys. Res.*, *89*(B7), 6256–6270, doi:10.1029/JB089iB07p06256.

Savage, J. C., and R. O. Burford (1973), Geodetic determination of relative plate motion in central California, *J. Geophys. Res.*, *78*(5), 832–845, doi:10.1029/JB078i005p00832.

Scharer, K. M., J. B. Salisbury, J. R. Arrowsmith, and T. K. Rockwell (2014), Southern San Andreas Fault evaluation field activity: Approaches to measuring small geomorphic offsets—Challenges and recommendations for active fault studies, *Seismol. Res. Lett.*, *85*(1), 68–76, doi:10.1785/0220130108.

Schellart, W., and G. Lister (2005), The role of the East Asian active margin in widespread extensional and strike-slip deformation in East Asia, *J. Geol. Soc.*, *162*(6), 959–972, doi:10.1144/0016-764904-112.
Schmidt, S., R. Hetzel, F. Mingorance, and V. A. Ramos (2011), Coseismic displacements and Holocene slip rates for two active thrust faults at the mountain front of the Andean Precordillera (33S), *Tectonics*, *30*, 1–15, doi:10.1029/2011TC002932.
Smedley, R. K., G. A. T. Duller, N. J. G. Pearce, and H. M. Roberts (2012), Determining the K-content of single-grains of feldspar for luminescence dating, *Radiat. Meas.*, *47*(9), 790–796, doi:10.1016/j.radmeas.2012.01.014.
Smedley, R. K., G. A. T. Duller, and H. M. Roberts (2015), Bleaching of the post-IR IRSL signal from individual grains of K-feldspar: Implications for single-grain dating, *Radiat. Meas.*, *79*, 33–42, doi:10.1016/j.radmeas.2015.06.003.
Smith, W. H. F., and P. Wessel (1990), Gridding with continuous curvature splines in tension, *Geophysics*, *55*(3), 293–305, doi:10.1190/1.1442837.
Stone, J. O. (2000), Air pressure and cosmogenic isotope production, *J. Geophys. Res.*, *105*(B10), 23,753–23,759.
Tapponnier, P., and P. Molnar (1976), Slip-line field theory and large-scale continental tectonics, *Nature*, *264*, 319–324.
Tapponnier, P., and P. Molnar (1977), Active faulting and tectonics in China, *J. Geophys. Res.*, *82*(20), 2905–2930, doi:10.1029/JB082i020p02905.
Thatcher, W. (2009), How the continents deform: The evidence from tectonic geodesy, *Annu. Rev. Earth Planet. Sci.*, *37*, 237–262, doi:10.1146/annurev.earth.031208.100035.
The Research Group on Active Fault System around Ordos Massif (1988), *Active Fault System Around Ordos Massif*, State Seismological Bureau [in Chinese], 335 pp., Seismological Press, Beijing.
Trauerstein, M., S. E. Lowick, F. Preusser, and F. Schlunegger (2014), Small aliquot and single grain IRSL and post-IR IRSL dating of fluvial and alluvial sediments from the Pativilca valley, Peru, *Quat. Geochronol.*, *22*, 163–174, doi:10.1016/j.quageo.2013.12.004.
Walker, R., and J. Jackson (2004), Active tectonics and late Cenozoic strain distribution in central and eastern Iran, *Tectonics*, *23*, TC5010, doi:10.1029/2003TC001529.
Wang, H., M. Liu, J. Cao, X. Shen, and G. Zhang (2011), Slip rates and seismic moment deficits on major active faults in mainland China, *J. Geophys. Res.*, *116*, B02405, doi:10.1029/2010JB007821.
Wang, Q., et al. (2001), Present-day crustal deformation in China constrained by Global Positioning System measurements, *Science*, *294*, 574–577, doi:10.1126/science.1063647.
Wesnousky, S. G. (2005), Active faulting in the Walker Lane, *Tectonics*, *24*(3), 1–35, doi:10.1029/2004TC001645.
Wesnousky, S. G., L. M. Jones, C. H. Scholz, and Q. Deng (1984), Historical seismicity and rates of crustal deformation along the margins of the Ordos block, North China, *Bull. Seismol. Soc. Am.*, *74*(5), 1767–1783.
Wesnousky, S. G., J. M. Bormann, C. Kreemer, W. C. Hammond, and J. N. Brune (2012), Neotectonics, geodesy, and seismic hazard in the Northern Walker Lane of Western North America: Thirty kilometers of crustal shear and no strike-slip?, *Earth Planet. Sci. Lett.*, *329–330*, 133–140, doi:10.1016/j.epsl.2012.02.018.
Wessel, P., W. H. F. Smith, R. Scharroo, J. Luis, and F. Wobbe (2013), Generic Mapping Tools: Improved version released, *Eos Trans. AGU*, *94*(45), 409–410, doi:10.1002/2013EO450001.
Wright, T. J., J. R. Elliott, H. Wang, and I. Ryder (2013), Earthquake cycle deformation and the Moho: Implications for the rheology of continental lithosphere, *Tectonophysics*, *609*, 504–523, doi:10.1016/j.tecto.2013.07.029.
Xu, S., A. B. Dougans, S. P. Freeman, C. Schnabel, and K. M. Wilcken (2010), Improved ^{10}Be and ^{26}Al-AMS with a 5MV spectrometer, *Nucl. Instrum. Methods Phys. Res., Sect. B*, *268*(7–8), 736–738, doi:10.1016/j.nimb.2009.10.018.
Xu, X., and Q. Deng (1990), The features of late Quaternary activity of the piedmont fault of Mt. Huoshan, Shanxi province and 1303 Hongdong earthquake (Ms=8) [in Chinese], *Seismolog. Geol.*, *12*(1), 21–32.
Xu, X., and X. Ma (1992), Geodynamics of the Shanxi Rift system, China, *Tectonophysics*, *208*(1–3), 325–340, doi:10.1016/0040-1951(92)90353-8.
Xu, X., Q. Deng, and H. You (1986), Evidence on dextral dislocation of fault at the western foothills of Mt. Xizhoushan, Shanxi province and its slip rate during the Holocene [in Chinese], *Seismolog. Geol.*, *8*(3), 44–46.
Xu, X., X. Ma, and Q. Deng (1993), Neotectonic activity along the Shanxi rift system, China, *Tectonophysics*, *219*(4), 305–325, doi:10.1016/0040-1951(93)90180-R.
Xu, X., G. Cheng, X. Ma, Y. Sun, and Z. Han (1994), Rotation model and dynamics of blocks in north China and its adjacent areas [in Chinese], *Earth Sci. J. China Univ. Geosci.*, *19*(2), 129–138.
Yu, S. (2004), A study on characteristics of tectonic block motion and tectonic setting of strong earthquakes in northern part of the Shanxi fault depression zone, *Acta Seismol. Sin.*, *17*(4), 417–425, doi:10.1007/s11589-004-0021-5.
Zhang, B., Y. Liao, S. Guo, R. E. Wallace, R. C. Bucknam, and T. C. Hanks (1986), Fault scarps related to the 1739 earthquake and seismicity of the Yinchuan Graben, Ningxia Huizu Zizhiqu, China, *Bull. Seismol. Soc. Am.*, *76*(5), 1253–1287.
Zhang, P., and W. Gan (2008), Combined model of rigid-block motion with continuous deformation: Patterns of present-day deformation in continental China, in *Investigations Into the Tectonics of the Tibetan Plateau*, edited by B. Burchfiel and E. Wang, *Geol. Soc. Am. Spec. Pap.*, *444*, 59–71, doi:10.1130/2008.2444(04).
Zhang, P., P. Molnar, B. C. Burchfiel, and L. Royden (1988), Bounds on the Holocene slip rate of the Haiyuan Fault, north-central China, *Quat. Res.*, *30*, 151–164.
Zhang, P., B. C. Burchfiel, P. Molnar, W. Zhang, D. Jiao, Q. Deng, Y. Wang, L. Royden, and F. Song (1990), Late Cenozoic tectonic evolution of the Ningxia-Hui Autonomous Region, China, *Geol. Soc. Am. Bull.*, *102*(11), 1484–1498, doi:10.1130/0016-7606(1990)102<1484:LCTEOT>2.3.CO;2.
Zhang, W., D. Jiao, P. Zhang, P. Molnar, B. C. Burchfiel, Q. Deng, Y. Wang, and F. Song (1987), Displacement along the Haiyuan Fault associated with the great 1920 Haiyuan, China, earthquake, *Bull. Seismol. Soc. Am.*, *77*(1), 117–131.
Zhang, Y., P. Vergèly, and J. Mercier (1995), Active faulting in and along the Qinling Range (China) inferred from SPOT imagery analysis and extrusion tectonics of south China, *Tectonophysics*, *243*, 69–95.
Zhang, Y., J. L. Mercier, and P. Vergèly (1998), Extension in the graben systems around the Ordos (China), and its contribution to the extrusion tectonics of south China with respect to Gobi-Mongolia, *Tectonophysics*, *285*, 41–75.
Zhao, B., Y. Huang, C. Zhang, W. Wang, K. Tan, and R. Du (2015), Crustal deformation on the Chinese mainland during 1998–2014 based on GPS data, *Geod. Geodyn.*, *6*(1), 7–15, doi:10.1016/j.geog.2014.12.006.
Zhou, M., T. Lü, Y. Zhang, and A. Ruan (2000), The geological structure background and the crustal structure in the northeastern margin of the Qinghai-Tibetan Plateau, *Acta Seismol. Sin.*, *13*(6), 687–697, doi:10.1007/s11589-000-0071-2.
Zhou, Y., B. Parsons, J. R. Elliott, I. Barisin, and R. T. Walker (2015), Assessing the ability of Pleiades stereo imagery to determine height changes in earthquakes: A case study for the El Mayor-Cucapah epicentral area, *J. Geophys. Res. Solid Earth*, *120*, 8793–8808, doi:10.1002/2015JB012358.